

## ABSTRACT

Title of Thesis: A STORM OF ACTIVITY: SUPER-RESOLUTION IMAGING ANALYSIS OF ACTIVITY-DEPENDENT SYNAPTIC DEVELOPMENT IN THE CIRCADIAN PHOTOENTRAINMENT CIRCUIT

Kyle Alexander Fisk, Master of Science, 2020

Thesis Directed By: Assistant Professor, Colenso M. Speer, Department of Biology

Circadian rhythmicity is a subconscious process that controls for many of our daily behaviors such as appetite and sleep. Controlled by the Suprachiasmatic Nucleus (SCN), the circadian rhythm is entrained to environmental light by a unique retinal ganglion cell, the intrinsically photosensitive retinal ganglion cell (ipRGC). Experience dependent activity has been shown to influence synaptogenesis and refinement of neural circuits. We utilized the ipRGC-SCN circuit to investigate activity-dependent changes in synaptic structure to understand the effect of activity on synaptogenesis throughout early development. We used the super-resolution microscopy technique, STochastic Optical Reconstruction Microscopy to quantify synaptic structural changes. We found reduced synaptic density and volume in activity manipulated animals compared to controls. These findings suggest ipRGC photoactivity is permissive to the proper development and signaling in ipRGC-SCN synapses. The proper activity-dependent maturation

of synapses in SCN neurons are crucial to the ability to normally photoentrain and maintain rhythmic bodily functions.

A STORM of activity: Super-resolution imaging analysis of activity-dependent synaptic development in the circadian photoentrainment circuit

by

Kyle Alexander Fisk

Thesis submitted to the Faculty of the Graduate School of the  
University of Maryland, College Park, in partial fulfillment  
of the requirements for the degree of  
Master of Science  
2020

Advisory Committee:  
Professor Colenso M. Speer, Chair  
Dr. Joshua H. Singer  
Dr. Elizabeth M. Quinlan

© Copyright by  
Kyle Alexander Fisk  
2020

**Dedication:**

To my wonderful fiancé, without whom I would not have had the inspiration and fortitude to achieve all my goals. A fierce advocate on my behalf, she has always supported my endeavors and been by my side through the trials and tribulations of graduate school life.

## Table of Contents

DEDICATION:.....	II
TABLE OF CONTENTS.....	III
LIST OF FIGURES AND TABLES: .....	IV
LIST OF ABBREVIATIONS.....	V
CHAPTER 1: CHARACTERIZATION OF SYNAPTIC MARKERS FOR STORM IMAGING IN THE SUPRACHIASMATIC NUCLEUS.....	1
Thesis Introduction .....	1
Introduction.....	7
Methods.....	16
Tissue Preparation.....	17
STORM Imaging .....	19
Results.....	22
Discussion .....	26
CHAPTER 2: QUANTITATIVE ANALYSIS OF ACTIVITY-DEPENDENT CHANGES IN SYNAPTIC STRUCTURE IN THE SUPRACHIASMATIC NUCLEUS .....	31
Introduction.....	31
Methods.....	36
Tissue Preparation.....	36
STORM Imaging .....	38
Results.....	41
Discussion.....	48
Thesis Discussion.....	51
BIBLIOGRAPHY .....	56

## List of Figures and Tables:

<b>Figure 1:</b> Diagram of STORM Sample Preparation	Pg 16
<b>Figure 2:</b> Manual Synapse Cluster Selection	Pg 23
<b>Figure 3:</b> Paired Synapse Quantification	Pg 25
<b>Table 1:</b> Antibodies Used For Immunohistological Characterization of SCN Synapses	Pg 26
<b>Figure 4:</b> Computational Filtering of Large Somatic Background Noise	Pg 42
<b>Figure 5:</b> STORM imaging of Wildtype and Double Knock-Out Synapses	Pg 43
<b>Figure 6:</b> Synaptic Density per Marker Across Development	Pg 44
<b>Figure 7:</b> Mean Synaptic Cluster Volume per Marker Across Development	Pg 45
<b>Figure 8:</b> Mean Synaptic Intensity per Marker Across Development	Pg 46
<b>Figure 9:</b> Volumetric Comparison of Synapses in the SCN	Pg 47

## **List of Abbreviations**

SCN – Suprachiasmatic Nucleus

ipRGC – intrinsically photosensitive Retinal Ganglion Cell

STORM – Stochastic Optical Reconstruction Microscopy

Opn4 – Melanopsin

PACAP – Pituitary Adenylate Cyclase Activating Peptide

VGLUT2 – Vesicular Glutamate Transporter 2

RHT – RetinoHypothalamic Tract

PSF – Point Spread Function

## **Chapter 1: Characterization of Synaptic Markers for STORM**

### **Imaging in the Suprachiasmatic Nucleus**

#### **Thesis Introduction**

Researchers have investigated the field of chronobiology since the 1950's and has since quickly become a large field — encompassing areas from cellular and molecular biology to behavior and psychology<sup>1,2</sup>. In everyday life, we subconsciously attune ourselves to a daily rhythm, controlling our appetite, mood, and sleep. Termed, the circadian rhythm, the detection of ambient light and control of neuroendocrine function is the basis of rhythmic physiology and behavior in both animals and plants<sup>3-5</sup>. The Suprachiasmatic Nucleus (SCN), comprised of about 20,000 neurons, is the main circadian center in mammals and is responsible for the maintenance of the circadian rhythm. The rhythm encoded by the SCN is additionally responsible for synchronizing connected brain centers to this rhythm<sup>6,7</sup>. Synchronization is able to be upheld even in the absence of environmental light through a transcriptional/translational feedback loop within the neurons of the SCN, encoding for an innate rhythm of, conveniently, approximately 24 hours and 11 minutes<sup>8,9</sup>.

Early observation of innate periodicity was discovered in fungi, paramecium, algae, and humans through experiments on temperature

regulation and behavior<sup>1,2,5</sup>. The finding of innate periodicity led many researchers, including Pittendrigh, to consider a genetic mechanism for the control of this rhythmicity<sup>1</sup>. However, it wasn't until the work of Ronald Konopka that the answer to genetic control of circadian rhythms was elucidated. Working in the lab of the renowned behavioral geneticist Seymour Benzer at Caltech, Konopka published a seminal paper showing two different x-chromosome mutations in *Drosophila* that lengthened and shortened the circadian period respectively<sup>10,11</sup>. Konopka induced point mutations in the genome, and after roughly 200 lines, found two mutations that produced a 19-hour and 28-hour circadian rhythm. Konopka named this gene the *period* (*Per*) gene, and subsequently it has been a major target reporter of circadian rhythmicity in cultured SCN explants. Using the discovery of this *Per* gene mutation, two groups (Jeffrey Hall and Michael Rosbash) went on to sequence the gene in 1984 and showed rise and fall of its expression throughout the day<sup>11-13</sup>. Notably, Michael Young also sequenced the *Per* gene; however, it was later in 1994 that Young found what is now known as the crucial pair to *Per*, completing the hypothesized feedback loop. Using *Drosophila* as well, Young named this protein *Timeless* (*tim*; known as *cryptochrome* (*cry*) in mammals) and showed two very important findings. First, the rhythmic expression of *tim* is dependent on expression of *Per*, and secondly that *tim* was necessary to transport *Per* to the nucleus in order to inhibit its own transcription<sup>14</sup>. Since these critical discoveries, other proteins have been implicated in the genetic feedback of the circadian rhythm such as

CLOCK, and BMAL1<sup>15</sup>. Discovered by Joseph Takahashi in 1997, the *Clock* gene, translated to the protein CLOCK, is necessary to turn on the expression of *per* and *tim/cry* through interaction in the nucleus of SCN neurons<sup>16</sup>.

Through the early work discerning the genetic control of circadian rhythmicity, we now know the key players are *per* and *tim/cry* interact together to control their own transcription creating a rise and fall throughout the day. In order to reinitiate the expression of these circadian genes, CLOCK/BMAL1 have been shown to turn on the transcription of *per* and *tim/cry* in the nucleus<sup>6</sup>.

With the understanding that circadian rhythmicity was under genetic control, but influenced by perceived light, the link between the retina and the SCN was the next crucial piece to be understood. Naturally one might think the traditional photoreceptors and their downstream circuitry led to changes in irradiance information being passed to the SCN. However, blind individuals have been documented to retain normal sleep/wake behaviors, maintaining synchrony to the environment despite lack of photoreceptor function<sup>17</sup>. Experiments in genetically engineered mice lacking the rod/cone photoreceptors also showed proper attunement to environmental light and melatonin suppression during perceived daylight<sup>8,18</sup>. This then points to the presence of a third, specialized photoreceptor for the control of circadian rhythms. The work of Hattar and Berson in the early 2000's uncovered the origins of the non-canonical photoreceptor in the ganglion cell layer of the retina<sup>19,20</sup>. These intrinsically photosensitive Retinal Ganglion Cells (ipRGCs)

utilize an invertebrate-like opsin, melanopsin, to detect blue shifted light and send excitatory signals to the SCN through glutamate neurotransmission<sup>17,21-23</sup>. In addition to glutamate, ipRGCs also make use of a secondary excitatory neurotransmitter, Pituitary Adenylate Cyclase Activating Peptide (PACAP). PACAP acts as a modulator to the primary glutamate neurotransmission during scotopic lighting (dusk and dawn)<sup>24-26</sup>. To extend the dynamic range of light activity signaled to the SCN, recent work has also shown the existence of a small subset of  $\gamma$ -aminobutyric Acid (GABA) releasing ipRGCs providing inhibitor signaling<sup>27</sup>. Thus far, these cells are the only known retinal cells to entrain the circadian clock to the environment. Since its discovery, Hattar and others have extended the depth of knowledge regarding ipRGCs and melanopsin and its effect on circadian biology<sup>28-31</sup>.

The SCN, as the central circadian center of the brain, makes many connections to other nuclei across the brain, as well as receives feedback from many others<sup>7,32,33</sup>. The most widely known, is the influence on the pineal gland and its regulation of melatonin and sleep. This phenomena is attributed to the feeling of jetlag and difficulties associated with overnight shift work, resulting in impaired cognitive ability, mood, and, obviously, sleep<sup>3,4,34,35</sup>. Altered signaling within the SCN and the activity of ipRGCs have also been implicated as precursors to bipolar disorders and neurodegenerative diseases such as Alzheimer's and Parkinson's. Melanopsin polymorphisms have been implicated in occurrence of Seasonal Affective Disorder (SAD). Additionally, chronic light disruptions during the subjective night can lead to the

susceptibility of developing cancers, metabolic disorders (i.e. type-2 diabetes), and cardiovascular disorders<sup>36-40</sup>. The ability of ipRGCs to accurately encode and communicate irradiance to the SCN is vital to sustained health and behavior.

The synapse is the fundamental unit of neuro-computation. Through signal transduction, excitatory or inhibitory, from one neuron to another, the brain interprets the input and computes the proper response. Changes in neuronal activity, typically tied to experience such as sight or smell, have been shown to alter the synaptic composition and firing patterns to their post-synaptic partners<sup>41-44</sup>. Studies manipulating the neuronal activity of experience dependent circuits have discovered negative effects ranging from weakened synaptic structure to drastic perturbations in axonal remodeling. Specifically, in studies of retinofugal projections of retinal ganglion cells to the dorsal Lateral Geniculate Nucleus (dLGN), axonal remodeling is drastically attenuate in an activity-dependent manner<sup>45-47</sup>.

It is crucial to be able to observe the changes in synapses responsible for photoentrainment in order to understand how the ipRGC-SCN circuit is altered in response to activity-dependent changes. Electron microscopy is the gold standard for the visualization of synapses, offering unmatched resolution. However, the main limitation of electron microscopy is the lack of molecular specificity. Pioneered in the early 2000's, super-resolution microscopy techniques were implemented to break the diffraction limit of light, achieving resolution orders of magnitude greater than previously possible<sup>48-</sup>

<sup>51</sup>. Super-resolution microscopy is able to utilize fluorescently labeled immuno-histochemistry to achieve molecular specificity as well as the level of resolution necessary to distinguish structural changes at a synaptic level. The SCN is an uncharted area in regard to super-resolution imaging and as such, adequate synaptic markers for optimal resolution have yet to be characterized. We hypothesized that excitatory pre- and post-synaptic markers would provide the optimal labeling efficiency for the visualization of synaptic structure given the excitatory signaling nature of ipRGCs to the retinorecipient region of the SCN.

In order to understand the possible pathology, it is crucial to understand the activity-dependent changes that occur at ipRGC-SCN synapse to ensure proper development and maintenance of this circuit. In the present study we focused on the activity-dependent changes in synapse structure of ipRGCs terminals in the retinorecipient region of the SCN throughout early post-natal development where the influence of activity on synapse formation is most prevalent. In order to manipulate activity, we eliminated the signaling ability of ipRGCs through the genetic ablation of melanopsin associated glutamatergic signaling and PACAP signaling. We observed and quantified the structures of retinorecipient synapses via super resolution imaging. The super resolution technique, Stochastic Optical Reconstruction Microscopy (STORM) allowed us to achieve a resolution high enough (~20nm) to discern pre- and post-synaptic clusters for quantification. We hypothesized that the number and size of synapses in activity-deprived

synapses would be dampened compared to controls, however not completely eliminated due to the maintained canonical photoreceptor signaling pathway.

## **Introduction**

Decades of research has shown the neural organization and Suprachiasmatic Nucleus (SCN) signal and how it's structure can coordinate the many rhythmic biological functions, including appetite, mood, and sleep. This includes work identifying the neuropeptides present in the SCN, the delineation of core and shell regions within the nucleus and the reciprocal signaling between them, and the cells responsible for the initial integration of light signaled from the retina<sup>7,16,17,33,52</sup>. While this vast amount of information allows better understanding of the SCN, it is at a cellular level. To date, there has been no prior work looking at the changes in signaling to the SCN at the synaptic level.

Recent work has targeted this question through the use of serial block face electron microscopy and an innovative approach to genetically targeting ipRGC input to the SCN. This careful reconstruction and analysis of multiple retinorecipient cells found a preference for retinal contact on the distal dendrites of retinorecipient neurons and within close proximity to dendrodendritic synapses between SCN cells<sup>53</sup>. While electron microscopy is

arguably the gold standard of synaptic imaging in terms of resolution, the major limitation of this methodology is the lack of molecular specificity.

Conventional fluorescent microscopy can provide molecular specificity through fluorescent proteins or antibody labeling; however, its resolution is limited by the diffraction of light. Questions involving the accurate observation and quantification of pre- and post-synaptic oppositions are not able to be performed using a diffraction limited imaging method. We aimed to characterize the activity-dependent changes throughout development in the SCN. Therefore, we utilized super-resolution microscopy to achieve high resolution images, clearly defining synaptic structure, while still maintaining molecular specificity. We set out to characterize synaptic scaffolding markers that would be sufficient for the detection of active zones and post-synaptic densities within the SCN. Additionally, it is known that ipRGCs are glutamatergic neurons that express Vesicular Glutamate Transporter 2 (VGLuT2)<sup>54</sup>. Therefore, we were able to accurately identify ipRGC pre-synapses in the SCN through the labeling of VGLuT2 vesicle pools. We hypothesized that, given the excitatory signaling nature of ipRGCs, similar pre- and post-synaptic proteins found in RGCs and their central targets would be found in SCN terminals alongside VGLuT2 clusters.

Microscopy has been used for centuries to observe and report biological structures and processes. Through the continued magnification of light by increasing and sophisticated arrays of lenses, scientists have been

able to visualize ever increasing complex structures. Just like the acuity of our own eyes however, there is a limit of how far one can magnify a biological sample before the waves of light blur and becomes indiscernible. When reduced to its most simplistic explanation, the limit to which an individual spot can be discerned is based on the size of the light intensity profile when the light wave is propagated through the optics of the microscope. In terms of practicality, this occurs when the intensity of light of two individual spots overlap enough to form one large spot of light in 3-dimensional space. The distribution of light intensity of a single spot is referred to as the Point Spread Function (PSF). Therefore, when the width of a molecules PSF overlaps with another, the intensity peaks overlap to produce a larger and wider PSF, thus decreasing the overall resolution. Therefore, the optimum resolution that can be achieved can be calculated by:

$$\frac{0.61 (\lambda)}{NA}$$

Where  $\lambda$  is the wavelength of light being used and NA is the Numerical Aperture of the objective. This optimum point of resolution is referred to as the diffraction limit or the Abbe limit. With a commonly used high NA objective of 1.40, the limit of resolution then becomes ~200nm in the x-y dimension<sup>55</sup>.

For most studies, the limit of resolution is rarely a complicating factor. For instance, studies of organ or tissue level research do not necessitate such magnification in order to observe and elucidate any outstanding

questions. These microscopy techniques are commonly referred to as conventional imaging techniques. Attempts to extend the limit of diffraction came in the way of confocal microscopy. While still being considered conventional imaging, confocal microscopy is a method in which further resolution is achieved by limiting out of focus background light so that only light in the plane of focus is collected. In doing so, the sample can be optically sectioned and produce a higher resolution 3-dimensional data set. This is done through the use of a pinhole to physically block the out of focus light in addition to raster scanning the sample with a focused laser such that the entire field of view is not illuminated at once<sup>55</sup>. Using these two tricks, confocal microscopy has been able to achieve the closest resolution to the diffraction limit while still being a “conventional” imaging approach.

In the early 2000’s groups began to establish intricate methods to break this current limit of resolution. These methodologies generally employ the theory of isolating two adjacent fluorescent molecules or manipulating the spatial frequency of fluorescent molecules in order to integrate their information towards a super-resolved image. Generally broken up into two categories, structural approaches or localization approaches, these techniques can garner at least 2x better resolution than conventional imaging. These approaches combine the use of fluorescent dye photo-physics and the manipulation of light in order to achieve the optimal illumination and collection of light intensities for the production of a super-resolved image<sup>56,57</sup>.

Structured Illumination Microscopy (SIM) is the only super-resolution method that does not utilize specialized fluorescent probes or individual molecule isolation. SIM achieves high resolution images by manipulating the structural frequency patterns of conventional images and deconvolution algorithms to limit the out of phase light being collected. This is done by illuminating the sample with stiped sinusoidal patterns in varying orientations to produce moiré fringes. This computational approach provides a 2x increase in resolution past the diffraction limit, allowing approximately 100nm lateral x, y resolution and 300nm axial z resolution. By saturating (Saturated SIM, or SSIM) the fluorescent intensities, the resultant images can produce higher spatial frequencies and thereby extend the level of deconvolution, thus achieving lateral resolution closer to 50nm<sup>56-58</sup>.

The second structural super-resolution methodology utilizes creative inspiration from confocal microscopy. Similar to confocal, Stimulated Emission Depletion (STED) microscopy raster scans the imaging field, however, instead of blocking out of focus light through the use of a pinhole, STED isolates individual fluorescent molecules through a specialized laser system. Through the use of an activation laser and a red-shifted donut-shaped “inactivation” laser, STED is able to force the molecules outside of the center, zero intensity spot, into a non-linear depletion ground state. This means that the width of the PSF of activated molecules at the center of the excitation laser will be reduced, thus allowing resolution past the diffraction limit. While achieving a resolution of ~30nm laterally and 30-40nm axially,

practically speaking, this also means the resolution is limited by the power output of the donut-shaped STED laser as both the inactivating STED laser and the excitation laser are both diffraction limited<sup>51,56,57</sup>.

The final two super-resolution techniques make use of biochemical characteristics of fluorescent molecules rather than physical manipulations of light to isolate the PSF of individual molecules. These techniques are both classified as Single Molecule Localization Microscopy (SMLM) methodologies. Both Stochastic Optical Reconstruction Microscopy (STORM) and Photo-Activated Localization Microscopy (PALM) take advantage of the photo-switching capabilities of certain fluorescent probes. The major difference between the two techniques is the use of photo-activated fluorescent proteins in the case of PALM, and photo-switchable dyes in the case of STORM. By stochastic activation to a light state and de-activation to a dark state, the imaging of each fluorescent molecule is spaced out over time instead of all at once in the case of conventional microscopy. Through the “blinking” nature of these photo-switching probes, this ensures that the probability of activating two neighboring molecules with overlapping PSFs at the same time is low. The centroid of the PSF can then be calculated to a gaussian fit, given the standard deviation of the PSF divided by the square root of the number of photons detected at that spot. By temporally spacing out adjacently activated molecules through stochastic activation, calculating the resultant centroid position, and reconstructing all identified molecules into a

single image, STORM and PALM can achieve resolutions of 15-20nm laterally<sup>48,49,56,59-61</sup>.

Achieving optimal STORM resolution relies on three main aspects of sample preparation, 1) photo-switching dye chemistry, 2) buffer composition, and 3) labeling density. The additional factors of spherical and chromatic aberrations caused by the objective lens and fluorescent probes respectively are negated through the imaging of fiducial bead fields and subsequent correction<sup>62-64</sup>.

The photo-switching ability of a dye is broken down and characterized by three additional metrics to identify optimal conditions for STORM imaging, the photon yield per activation to its 'on' state, the number of cycles a dye can switch between the off-and-on state (recovery fraction), and the duty cycle, or the fraction of time spent in the 'on' state. As the theory of STORM necessitates a very bright molecule that is isolated from adjacent molecules, the optimal dye would be characterized by having a high photon count per switching event, a high switching cycle count (for increased accuracy in estimating the localization precision), and a low duty cycle<sup>62</sup>. Importantly, these characteristics are influenced by the amount of laser power used to illuminate these photoswitchable probes. The relationship between photon emission and the off-switching rate is linear with respect to excitation intensity for almost all dyes (Cy3B is the only exception), meaning, faster switching and higher photon emission leads to increased resolution.

These dye chemistry characteristics are also aided by the composition of the buffer they are imaged in. Prior work has shown the optimal buffer additions necessary for quality and sustained photo-switching. The addition of a thiol to the polymethine bridge of the cyanine dye forces a conversion to a dark state has been shown to improve the photo-switching ability of the dye. Additionally, to increase photon detection, work has shown the addition of the oxygen scavenger, Glucose Oxidase (GLOX), increased the number of cycles and photon yield per cycle by reducing triplet state inactivation of the fluorescent probe. Thus, the optimal imaging buffer utilizes a thiol, such as methylethylamine, and an oxygen scavenging system such as GLOX<sup>62,63</sup>.

Finally, the labeling density of the sample can affect the resultant resolution of the image. Nyquist sampling dictates the image sampling interval be smaller than half of the desired spatial resolution<sup>65</sup>. This therefore means an increase in the number of photons detected per second will increase the overall resolution. In terms of labeling density, this means fluorophores activated simultaneously in too close of proximity to each other with low photon yields will not have their spatial resolutions preserved, thus losing overall image resolution. The labeling density can be affected by the primary antibody affinity as well as the thickness of the tissue being imaged. Too sparse of density will result in an incomplete structure being represented in the final image, whereas, too dense of a label can lead to many overlapping PSFs being active at the same time, thus not being able to isolate the centroid positions of these molecules. These are controlled for via label

concentration optimization, tissue thickness optimization, and the use of total internal reflectance (TIRF). TIRF is a physical manipulation of the angle in which light enters the objective to illuminate the sample. This angle, termed the critical angle, is the point at which a ray of light is “trapped” between the differing refractive indexes of the immersion oil and the sample. This exact point causes an evanescent wave of light in the z dimension that decays exponentially, thus greatly illuminating only the closest molecules to the sample surface. As such, this decreases background illumination while increasing the intensity of those molecules in proximity of the evanescent illumination<sup>59,61,66</sup>. Luckily, prior work has tabulated a long list of STORM dyes in detail across the color spectrum as well as established the proper buffer conditions necessary for optimal STORM imaging. The challenge that remained was the identification of molecular labels with sufficient density to accurately detect synapses within the SCN<sup>62</sup>.

There have been studies using conventional microscopy approaches to characterize synaptic innervations in the SCN<sup>67</sup>. Various other studies have shown quality staining of pre- and post-synaptic scaffolding markers using STORM in both the retina and main olfactory bulb of the mouse. However, up to this point, super-resolution studies have not been conducted in the SCN. Therefore, no prior literature has described synaptic molecular markers with sufficient labeling density to accurately demarcate the structure of pre- and post-synaptic scaffolding structures. We hypothesized that, given the classification of ipRGCs as retinal ganglion cells (RGC), the structure and

scaffolding proteins associated with pre- and post-synaptic terminals would follow that of other, previously described RGCs and follow that of previously described markers in conventional studies.

## **Methods**

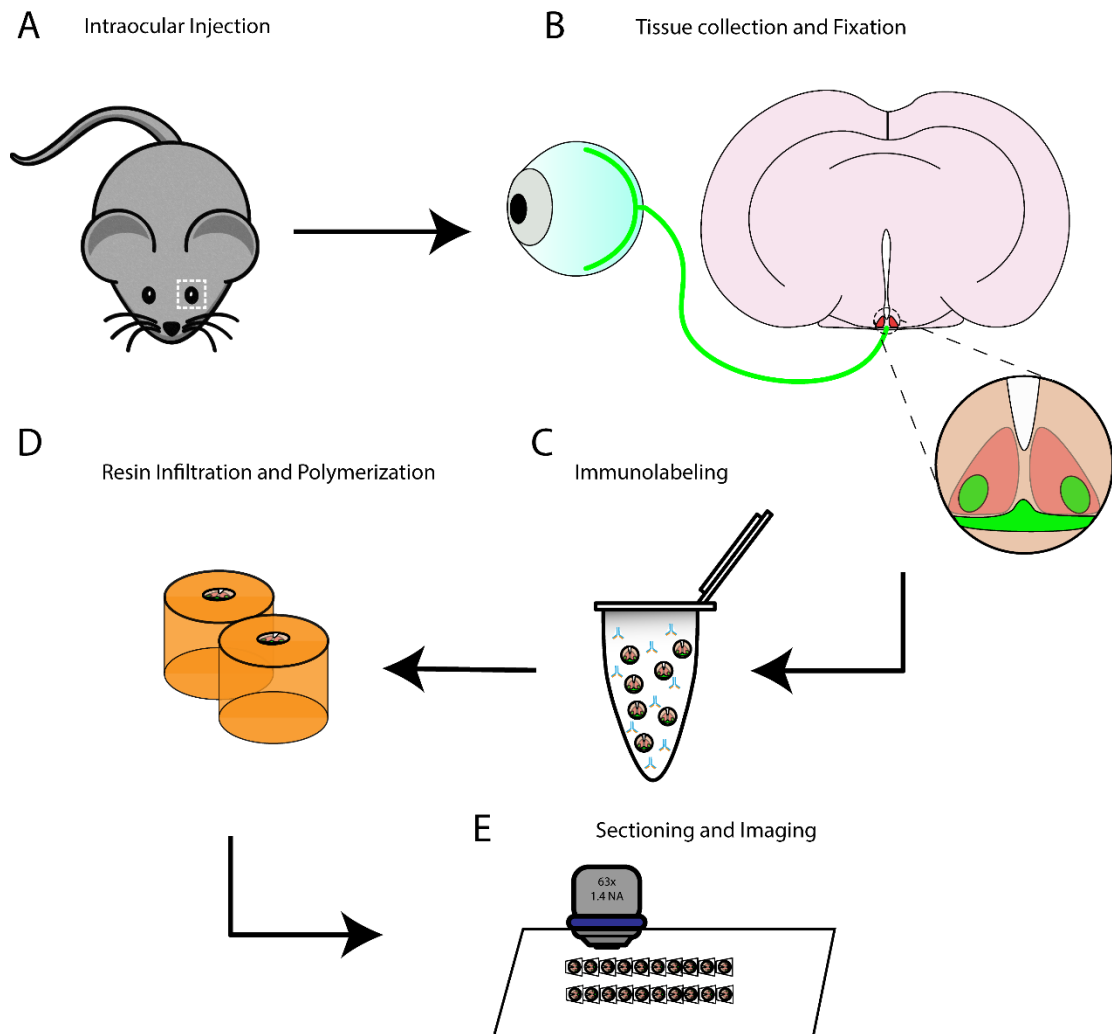


**Figure 1. Diagram of STORM sample preparation**

Samples were processed for STORM imaging using genetically identified mice (A) by histological sectioning and microdissection of the SCN (B), followed by immunolabeling (C) and resin infiltration and ultramicrotomy (D). Volumetric arrays were then imaging using a custom STORM microscope (E).

## Tissue Preparation

### *Animals*

Animals were acquired from Dr. Samer Hattar (Opn4<sup>cre/cre</sup> 68) and Drs. Brad Lowell and Rachel Ross (PACAP<sup>fl/fl</sup> 69) and kept in 12/12 LD light cycles with access to food and water ad libidum. Animal handling and experiments were performed in accordance with protocols approved by the University of Maryland Institutional Animal Care and Use Committee standards. Tissue was collected from mice at three developmental time points (postnatal days 8, 15, and ~60).

Animal breeding was established to generate littermate controls in all experiments by crossing double homozygous Opn4 / PACAP knock-out animals with double heterozygous Opn4 / PACAP conditional control animals. In doing so, this would produce an expected litter with equal probability of double knock-out and double heterozygous animals.

### *Eye Injections & Perfusion*

One day prior to tissue collection, retinofugal projections were labeled using fluorescent anterograde tracing to enable fluorescence-guided microdissection of the SCN. Upon perfection of localizing the SCN in slice, microdissection was moved to a label free detection. Animals were maintained under anesthesia with isoflurane inhalation through a nose cone apparatus and a roughly 0.3mm puncture was made at the scleral margin of

the eye. The anterograde tracer, Cholera Toxin Beta-subunit conjugated to Alexa-488 (Sigma) was injected into the vitreal space, and animals were returned to their cages. Animals at postnatal day 7 underwent careful surgical opening of the eyelid in order to access the eye for injection. 16-24 hours later, animals received a single IP injection of 20mg/kg ketamine/xylazine mixture. Animals were intracardially perfused with 0.9% saline (0.9-1.1mL/min, 10-15mLs total) followed by 15-20mL of 4% paraformaldehyde in 0.9% saline. Brain and retinae were dissected and post-fixed for 1 hour in 4% PFA at room temperature (Fig. 1a).

#### *Tissue slicing and screening*

Brains were embedded in 2.5% low-melt agarose and placed on ice to solidify. Brains were sliced in ice cold conditions at 60µm using a Leica VT1000 vibratome. Slices were then screened using an Olympus fluorescent dissecting scope to identify CTB-488(+) signal within the SCN; the two SCNs were removed using a 500um diameter circular punch using a blunt-edged needle (Fig. 1b).

#### *Immunohistochemistry*

Tissue punches were blocked in 10% Donkey-serum with 0.01% Sodium Azide and 0.25% Triton X-100 for 1-1.5 hours at room temperature then incubated in primary antibodies for 2-3 days at 4°C (Ms Bassoon, Rb Homer1, Gp VGlut2). Following primary antibody incubation, tissue was

washed 4-5 times in 1xPBS for 20 minutes each and incubated in secondary antibodies overnight at 4°C (Dk anti-Ms DyLight 749P1, Dk anti-Rb Alexa-647, Dk anti-Gp Cy3B). Tissue was then washed 4-5 times in 1xPBS for 20 minutes each and incubated in a lectin stain, wheat germ agglutinin conjugated to Alexa-488, overnight at 4°C to label cytoarchitecture (Fig. 1c).

### STORM Imaging

#### *Resin polymerization and ultrasectioning*

Following WGA staining, tissue was washed in 1xPBS 2 times for 20 minutes and post-fixed in 3% paraformaldehyde / 0.1% glutaraldehyde in 1xPBS for 2-3 hours at room temperature. Tissue was then washed 3 times in 1xPBS for 20 minutes each, followed by graded ethanol dehydration series, 50%, 75%, 95%, 100%, 100%, for 20 minutes each. Dehydrated tissue was then infiltrated with Ultrabed Epoxy Resin (EMS) in increasing ratios diluted in 100% ethanol (2:1 overnight, 1:1 for 2 hours, 100% resin twice for 2 hours). Upon embedment in BEEM capsules (EMS), blocks were cured in a 70°C oven for 16-18 hours (Fig. 1d).

#### *Ultrasectioning*

Cured samples were trimmed and sectioned on a Leica UC7 ultramicrotome. Blocks were trimmed using a diamond trim tool from Diatome and sections collected using a JumboHisto diamond also from diatome. Ultrathin sections were collected at 70nm onto coverslips coated with 0.5%

gelatin / 0.05% chromium potassium sulfate. Coverslips containing sections were dried on a hot plate at 60°C to bond sections to the coverslip (Fig. 1e).

### *STORM Dyes*

Custom STORM secondary antibody dyes were conjugated with corresponding species specificity to primary antibody host species. Previously quantified high quality STORM reporter probes (Atto 488, Cy3B, Alexa 647, DyLight 749P1) along with an activator probe, Alexa 405, were incubated in 80µL of respective IgG antibody, 10µL sodium bicarbonate, 2.2µL respective reporter probe, and 1.3µL activator probe for 20 minutes in a light sealed container. The resultant conjugated antibodies are then purified using a NAP-5 Sephadex column (GE Healthcare).

### *STORM acquisition and analysis*

Samples were prepared for STORM imaging via exposing photoswitching sites by chemically etching the resin and sealing into a flow chamber filled with STORM imaging buffer. Etching was achieved by incubation in 10% sodium ethoxide (NaEtOH) for 5 minutes. Excess NaEtOH was rinsed with 95% ethanol to prevent precipitation. Fluorescent beads (540/560 and 715/755 mixture) in two different concentrations were spotted to serve as fiducial markers for chromatic aberration and flat field illumination corrections. Once the coverglass was adhered to a microscope slide using

double sided tape, a STORM imaging buffer consisting of 10% glucose, 17.5 $\mu$ M glucose oxidase, 708nM catalase, 10mM mercaptoethylamine, 10mM NaCl, and 200mM Tris was flowed in and sealed with epoxy.

Image acquisition was performed using a custom built TIRF system through an inverted Nikon Ti confocal stand with a Nikon 60x 1.4NA TIRF objective. The corresponding lasers used for excitation were 488nm, 561nm, 647nm, and 750nm lines with a 405nm laser for secondary activation of far red (Alexa 647 and DyLight 750P1) STORM probes. Images were collected on a Hamamatsu Orca Flash CMOS camera with an overall field size of 96x96 $\mu$ m.

Using a Python based open source automated image acquisition software (Zhuang Lab GitHub), samples were tiled using a 4x 0.9NA objective and to achieve relative spatial position, then further tiled at 60x magnification to identify ROIs for image acquisition. Once ROIs were established, conventional resolution images were taken at each selected ROI, followed by STORM acquisition. The length of STORM imaging in each channel varied based on the signal in each respective wavelength; 750 contained 7000-8000 frames, 647 contained 7000-8000 frames, 561 contained 8000 frames. STORM analysis was performed using the open source DAOSTORM algorithm to calculate the centroid positions of individual molecules<sup>49</sup>. The corresponding molecule list was transformed to correct for chromatic aberrations caused by the imaging objective and flat field illuminance aberrations by using the transformation maps generated by bead images.

Volumetric reconstruction of sections was achieved by alignment of adjacent sections using the WGA channel. The alignment algorithms (Fiji Processes) used were initially, the Scale-Invariant Feature Transform (SIFT) rigid alignment<sup>70</sup>, followed by elastic block matching alignment<sup>71</sup>. While the algorithms were sourced matched on adjacent sections, the parameters for transformation were applied through the volumetric stack.

## **Results**

The projections of ipRGCs to the SCN were initially identified using anterograde tracing of CTB-488. Adult C57Bl/J6 animals (p30-p60) were utilized to test the labeling efficacy of synaptic markers in the retinorecipient region of the SCN as functionally mature synapses can adequately report complete or incomplete labeling. STORM imaging parameters such as buffer conditions, TIRF angle, and laser power, were optimized in this region and each synaptic marker was tested using these parameters. Optimization challenges that were overcome in the process of evaluating ideal immunolabeling of synaptic proteins included the reduction in background noise, standardizing optimal single molecule fitting parameters, and standardizing optimal volumetric stack alignment parameters. Synaptic staining quality was initially analyzed using volumetrically aligned STORM stacks based on three factors: (1) characteristic oblong shape comparable to those seen in prior synaptic super-resolution studies, (2) continuity of these structures across multiple sections, corresponding to real signal as opposed

to artifact, and (3) identified molecule counts above 500 using visualization software, Insight 3. Identified clusters that exhibited each of these criteria were considered good synaptic markers for reliable labeling of pre- and post-synaptic oppositions within the SCN. Synaptic markers that did not meet these characteristics, and were therefore rejected, typically did not meet two out of three characterization parameters. A lack of continuity across sections and lack of clusters significant against background noise were automatically grounds for exclusion. The synaptic markers that met all three inclusion criteria were the pre-synaptic proteins, Munc13-1 and Bassoon; the post-synaptic markers, Homer1 and PSD-95; and both excitatory glutamate vesicle transporter protein, VGluT2. In order to distinguish synaptic markers, the species specificity of each antibody was necessary to consider. For this reason, further tests were conducted to ascertain the optimal markers that do not have species cross-reactivity. We identified Ms-Bassoon (Synaptic Systems), Rb-Homer1/2/3 (Synaptic Systems), and Gp-VGluT2 (EMD-Millipore) as the optimal pairing for the identification of synapses within the SCN. These successfully identified synaptic markers will provide the basis for accurate synapse identification and further synaptic metrics.

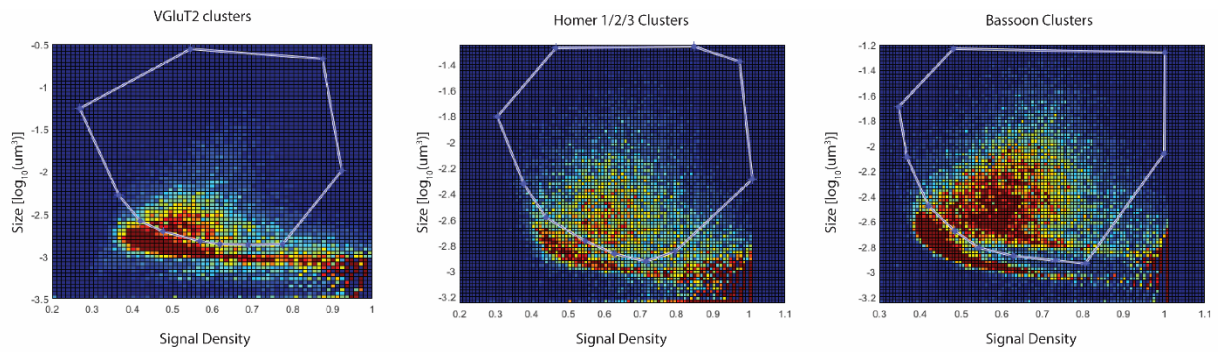


**Figure 2. Manual Synapse Cluster Selection**

Through pixel blurring and Otsu-thresholding clusters were able to be manually separated by size into synaptic and non-synaptic classes for further analysis.

The resulting STORM images acquired using our selected synaptic markers were further analyzed utilizing a series of thresholds and connected component analyses to assure accurate identification of paired synapses. Fitted STORM clusters were separated from background and assigned as synaptic or non-synaptic clusters through an automated MATLAB segmentation analysis (Fig. 2). Pixel blurring and otsu-thresholding of clusters was performed to accurately identify objects that are connected components and plotted as a size vs intensity heatmap. These calculations allow for the data to be parsed into two separate size classes, synaptic and non-synaptic. The resulting synaptic objects can then be further analyzed using a shell analysis to ascertain the presence of identified clusters of a separate imaging channel within the shell. Identified clusters within the shell analysis of separate channels are deemed as paired pre- and post-synaptic structures. These paired structures are then able to be quantified for the overall number of paired synapses, the size (in nm<sup>3</sup>) of identified synaptic clusters, and the intensity of these clusters (Fig. 3).

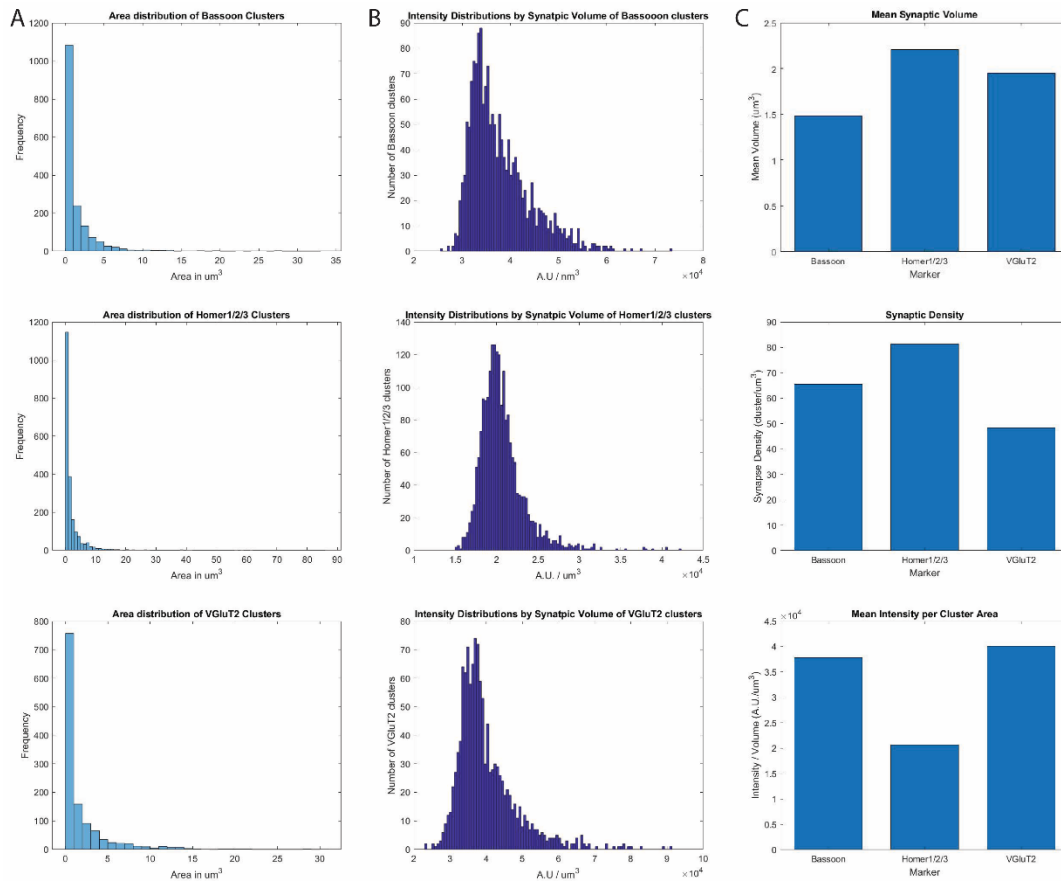


### Figure 3. Paired Synapse Quantification

Proof of concept quantification of optimal synaptic markers. A) Histogram distributions of synaptic marker volume in  $\mu\text{m}^3$ . B) Synaptic cluster intensity measurements per cluster volume. C) Calculated mean values for synaptic volume, synaptic density, and intensity per cluster broken up by synaptic marker.

Protein	Species	Company
PSD-95	Ms	ThermoFisher/Invitrogen
PSD-95	Ms	Synaptic Systems
PSD-95	Rb	Synaptic Systems
Homer1a	Rb	Synaptic Systems
Homer1/2/3	Rb	Synaptic Systems
Bassoon	Gp	Synaptic Systems
Bassoon	Rb	Synaptic Systems
Bassoon	Ms	Synaptic Systems
Piccolo	Rb	Synaptic Systems
SHANK1/2/3	Ms	Santa Cruz
VGluT2	Gp	Millipore
VGluT2	Rb	Synaptic Systems
ERC1/2	Rb	Synaptic Systems
Munc13-1	Rb	Synaptic Systems
Munc13-1	Ms	Synaptic Systems
Munc13-1	Gp	Synaptic Systems
SAP102	Rb	Synaptic Systems

Table 1. **Antibodies used for immunohistochemical characterization of SCN synapses**  
Table 1 shows a complete list of all antibodies tested for labeling of synaptic structures in the SCN. Antibodies meeting labeling criterion and selected for further studies are highlighted.

## **Discussion**

The SCN has been studied extensively on a cellular and physiological level for many years and further analysis using super-resolution imaging provides additional understanding into the changes in synaptic dynamics aiding circadian rhythmicity<sup>9,19,33,72</sup>. Through careful analysis of 9 different synaptic proteins of differing species specificity combinations, we have narrowed the field of synaptic markers to one pre- and post-synaptic marker

and one marker of VGluT2 that were then optimized for high quality STORM imaging. Bassoon and Homer synaptic markers are large components of the active zone (AZ) and post-synaptic density (PSD) respectively and make for ideal delineators of pre- and post-synaptic ends of the synapse<sup>73,74</sup>. Bassoon is a member of the pre-synaptic machinery involved in the maintenance and structure of the AZ as well as vesicle priming. Importantly Bassoon has been implicated in activity-dependent communication between the pre-synaptic bouton and the nucleus during development<sup>74,75</sup>. On the opposite side of the synapse, the marker we found to work most optimally targets all three isoforms of Homer. Known to be found in glutamatergic neurons Homer acts as a scaffolding protein allowing for the anchoring of post-synaptic machinery such as NMDA and metabotropic Glutamate receptors. Much like bassoon, Homer has also been implicated to be regulated in an activity-dependent manner<sup>76-78</sup>. With established synaptic markers that have regulatory roles in synaptic activity, the maturation and activity-dependent changes in the SCN will be able to be observed.

While we show here optimized labeling of synaptic markers in the SCN, these markers were focused on previously validated markers in either the retina or other brain nuclei<sup>79,80</sup>. As such there are further synaptic markers that could be explored. For example, investigation into synaptic changes in reciprocal feedback would necessitate validating inhibitory synaptic markers as nearly all neurons in the SCN are GABAergic<sup>81</sup>. Additionally, there has been evidence of an ipRGC subtype that provides GABAergic stimulation to

retinorecipient neurons<sup>27</sup>. Recent progress in the field of translomics and axonal ribo-Tag methodology can be an excellent resource for the targeting of actively translated proteins for STORM imaging<sup>82</sup>. The combination of a local translome and STORM visualization of identified proteins can probe questions related to local synaptic organization during development and plasticity.

It is important to consider the time frame and experimental process of STORM imaging and how it compares to other techniques in answering the same questions related to synaptic structure. One of the major limitations to STORM imaging in large volumes is the significant time investment, necessitating approximately two weeks from tissue harvest to analysis of images. As such, widespread screening for synaptic marker efficacy can be burdensome. A parallel approach to quickly screen for synaptic marker presence can be to increase the resolution by physically increasing the size of the structure you're observing. A recently developed methodology achieves this by infiltrating the tissue with an elastic polymer, binding labeled structures, and physically expanding the tissue. Thusly termed Expansion Microscopy (ExM), this technique can achieve similar resolution to SSIM (~70nm laterally and 200nm axially) in roughly half the time necessitated for STORM processing<sup>83,84</sup>. While achieving a more efficient processing time, ExM does not reach the level of resolution STORM can achieve and thus, its use should be limited to large scale screening scenarios or experiments that involve questions of synapse localization.

At the current moment, due to limitations of antibody labeling species compatibilities and spectral overlap of laser line wavelengths, most STORM systems can only collect data from 4-color imaging experiments. Recent work by Ralf Jungmann and others have successfully shown the ability to achieve single-molecule localizations of fluorescently labeled DNA strand binding events<sup>85,86</sup>. Instead of utilizing the photokinetic nature of STORM probes to stochastically blink from a dark state to a light state, DNA-PAINT relies on transient, reversible DNA probe binding events that bring fluorescent-labeled probes into the plane of focus. As each fluorescent signal is dependent on a single binding event, it is possible to achieve 10-color imaging by observing the binding events of individual secondary DNA strands sequentially and recombining the data into one aligned image<sup>87</sup>. In the future, identified proteins of interest discovered by local translomics can be combined with DNA-PAINT imaging to provide a highly multiplexed visualization of sub-synaptic organization. This multiplexed imaging technique can enable for the spatiotemporal analysis of proteins/mRNA during changes in circadian phase protein expression or following activity manipulations.

In summary, through careful analysis, we have identified pre- and post-synaptic antibody markers in addition to VGlut2 antibody markers for the identification of ipRGC terminals in the SCN. Prior to this study, STORM synaptic imaging has not been described in the SCN. The identification of synaptic labeling in the SCN can further be used to answer questions of synaptic circuitry in the circadian system.



## **Chapter 2: Quantitative Analysis of Activity-Dependent Changes in Synaptic Structure in the Suprachiasmatic Nucleus**

### **Introduction**

Made up of ~20,000 neurons, the Suprachiasmatic Nucleus (SCN) is the central coordinator of daily biological processes and rhythms<sup>6,16,33</sup>. The SCN is able to achieve this task by maintaining innate reciprocal signaling within itself through transcriptional/translational feedback loops between its ventrolateral core and dorsomedial shell regions, irrespective of outside signaling<sup>7,9,88-90</sup>. This rhythmic expression is communicated to multiple brain regions controlling various behavior outputs such as, rest and activity (sub Paraventricular Zone), temperature (Preoptic Area), and appetite (Paraventricular Nucleus)<sup>52,91</sup>. Interestingly, in recent years, neurological diseases have been linked to the ability of light to entrain the circadian system, while other disorders have been attributed to circadian disruptions<sup>91,92</sup>. Most commonly known disorders involving circadian disruptions are the feeling of jetlag and Seasonal Affective Disorder (SAD)<sup>3,34,38,93</sup>. Further evidence has also shown the correlation of disruption to the onset of diabetes, cardiovascular disease, and cancers<sup>32,94</sup>. Finally, neurological diseases such as Parkinson's and Alzheimer's disease have been linked to the degradation of retinal circuitry and onset of circadian disorders<sup>36,37,39</sup>. Critically, all of these disorders are linked to ipRGC activity

and its ability to convey light signals in order to entrain the SCN<sup>95</sup>. Due to the wide breadth of brain regions that the circadian center signals to, changes or abnormalities to the synaptic structure and function can explain varying cognitive, physiological, and behavioral outcomes. It is important to understand how differing ipRGC activity can affect synaptic structure in the SCN and its implications on further signaling within the brain.

To explore the activity-dependent changes in the SCN, we must understand how activity is signaled in ipRGCs. Discovered by Hattar and Berson in the early 2000's, ipRGCs have become known as the crucial communicator of environmental light to photoentrain the circadian system<sup>19,20</sup>. IpRGCs accomplish their intrinsic photosensitivity through the protein melanopsin. Related to invertebrate opsins, melanopsin is a rhabdomeric type photoreceptor responsive to blue wavelengths (~480nm) that activates a Gq-mediated signaling cascade causing a transient increase in cytosolic Ca<sup>2++</sup> levels via transient receptor potential (TRP) channels<sup>17,28,96,97</sup>. Melanopsin itself is uniformly distributed throughout the cell, unlike traditional rods and cones that are compartmentalized, and have been recorded to have single photon responses<sup>17,98,99</sup>. The combination of high photon sensitivity with G-protein mediated activation and diffuse protein expression combine to produce a slow and sustained response to light<sup>19,100</sup>. This depolarization causes the release of glutamate and Pituitary Adenylate Cyclase Activating Peptide (PACAP) onto retinorecipient neurons in the core region of the SCN through the retinohypothalamic tract (RHT)<sup>24,25,101,102</sup>. These retinorecipient

neurons express vasoactive intestinal peptide (VIP) and are the initiators of circadian phase resetting in response to light<sup>103–105</sup>. The primary excitatory signal for light signaling is glutamatergic acting through the canonical NMDA and AMPA receptors on VIPergic neurons within the SCN<sup>54,104</sup>. PACAP signaling is used as a modulator of glutamatergic signal during scotopic lighting and acts through the PAC1 receptor<sup>26</sup>. The excitatory drive of ipRGC glutamatergic neurotransmission allows for Ca<sup>2+</sup> influx and activation of the cAMP response element-binding (CREB) pathway to induce new transcription of *Per* genes, thus signaling the start of the circadian cycle<sup>6,7</sup>. These functional aspects of melanopsin and ipRGCs signaling are considered the main avenue for the entrainment of the circadian system in an activity dependent manner.

It is important to consider, despite being considered the third photoreceptor of the retina, ipRGCs are still involved in the canonical retinal ganglion cell circuitry within the retina, including rod and cone photoreception signal integration<sup>17,19,20</sup>. As such, ipRGCs participate in the early developmental activity dance known as retinal waves<sup>106</sup>. As the name suggests, waves of coordinated activity travel across the retina, sending action potentials to central brain targets and inducing synaptogenesis<sup>107–110</sup>. Throughout retinal development, retinal wave activity changes in its pattern of activity, being classified into three distinct phases. The first phase is pre-natal and is characterized by signaling between retinal ganglion cells via gap junctions. Immediately post-natal until p11, these “early-stage” waves are

coordinated through nicotinic acetylcholine receptor activation<sup>111–115</sup>. The “late-stage” waves in mice, approximately p11 to p21, are primarily ionotropic glutamate receptor activation from bipolar cells onto RGCs, as well as a switch from nicotinic to muscarinic acetylcholine receptors<sup>111,116,117</sup>. A large body of literature has focused on characterizing retinal waves and their effect on downstream synaptic organization. The initiation of early-stage retinal waves is thought to be spontaneous  $\text{Ca}^{++}$  spikes of Starburst Amacrine Cells (SACs) that propagate via recurrent excitatory connections. Correlated multi-electrode array recording and  $\text{Ca}^{++}$  imaging experiments have shown these spontaneous events have a refractory period of approximately 1-2 minutes in early stage waves and 1 minute in late stage waves<sup>106,114,118</sup>. These lengthy refractory periods create functional boundaries that constrain the boundaries of these waves, which in turn create locally correlated RGC activity patterns. Manipulations of retinal wave activity have shown the altered organization of retinogeniculate and retinocollicular synaptic targets<sup>112,119,120</sup>. The genetic deletion of the B2 subunit of nicotinic AcetylCholine Receptors (nAChR) or repeated epibatidine exposure to block early-stage nicotinic retinal waves greatly reduces the activity-dependent refinement of eye-specific projections within these regions<sup>111,120–122</sup>. Importantly, in murine development, canonical photoreceptor opsins are not active due to the closure of the eyelid until around post-natal day 12, and therefore cannot contribute to the activity-dependent development of retinofugal projections. Melanopsin, however, has been shown to be responsive to light cues in utero and from birth at

p0<sup>31,100,123,124</sup>. Therefore, the early post-natal activity of ipRGCs incorporates early-stage retinal wave activity as well as environmental light activity through melanopsin. Upon eye opening, ipRGC activity is expanded and modified to now include traditional rod and cone photoreceptor input as well as switch from early-stage to late-stage retinal wave activity.

Overwhelming evidence has shown coordinated activity to induce synaptogenesis and activity-dependent refinement of synapses<sup>125–128</sup>. Upon activation, post-synaptic densities open Ca<sup>++</sup> channels and NMDA receptors are recruited to the post-synaptic membrane, followed by scaffolding molecules (PSD95, Homer1, actin polymerization) and further receptor recruitment (AMPA receptors)<sup>129–134</sup>. In early development synaptic connections are characterized by large quantities of small synapses. Upon increased synaptic activity and maturation, selected synapses are either pruned or strengthened leading to fewer and structurally larger synapses<sup>44,135,136</sup>. The increase in post-synaptic structural organization has been shown to correlate to synaptic strength. Glutamate uncaging experiments have been shown to increase the dendritic spine size as a function of uncaging events<sup>125,137–139</sup>. The structural changes in synaptic size as a function of synaptic strength have primarily been studied within the hippocampus, however, the mechanisms of activity-dependent synaptic development in the SCN remains poorly understood.

To observe changes in activity-dependent synaptic structure, we utilized volumetric STORM imaging to quantify how synaptic volume changes

through development and in response to activity perturbations. Using the previously described synaptic markers of Bassoon (pre-synaptic), Homer1/2/3 (post-synaptic), and VGlut2 (pre-synaptic Glutamatergic vesicle pool), we are able to volumetrically reconstruct ~10um worth of SCN for synaptic analysis. In order to manipulate ipRGC activity to the SCN, we selectively bred a double knock-out (dKO) mouse line targeting melanopsin (Opn4) and PACAP. This dKO model selectively ablates activity originating from ipRGC/melanopsin photoreception. We hypothesized that manipulations to activity in ipRGC signaling would significantly decrease the number and size of synapses across development; however not to the extent of near elimination due to the survival of rod and cone signaling through ipRGCs.

## **Methods**

### Tissue Preparation

#### *Animals*

Animals were acquired from Jackson Labs and kept in 12/12 LD light cycles with access to food and water ad libidum. Experimental double Knock-Out animals were selectively bred by crossbreeding Opn4<sup>cre/+</sup> and PACAP<sup>fl/+</sup> animals to produce a Opn4<sup>cre/cre</sup>/PACAP<sup>fl/fl</sup> x Opn4<sup>cre/+</sup>/PACAP<sup>fl/+</sup> mating pair, ensuring 50% probability of experimental and littermate control offspring<sup>68,69</sup>. Experiments were performed adult animals ages p8, p15, and >p60. Animal handling and experiments were performed in accordance with the University of Maryland Institutional Animal Care and Use Committee standards.

### *Eye Injections & Perfusion*

Animals were maintained under anesthesia with isoflurane inhalation through a nose cone apparatus and a roughly 0.3mm puncture was made at the scleral margin of the eye. The anterograde tracer, Cholera Toxin Beta conjugated to Alexa-488 (Sigma) was intraocularly injected, and animals were returned to their cages for 16-18hours until sacrifice. At the time of sacrifice, animals were lethally anesthetized with a ketamine/xylazine mixture and allowed to sedate until no flinch response was noted. The animal then had its chest cavity surgically opened to expose the heart, a 32.5G butterfly needle was inserted into the left ventricle, and the right atrium eviscerated to allow blood to flow out of the vasculature. The animal was flushed with 10-15mL of 0.9% saline with a flow rate of 0.9-1.1mL/min using a syringe pump until the discharge was clear. Once clear, the animal was perfused with 15-20mL of 4% paraformaldehyde. Immediately following, the brain was dissected out and post-fixed for 1 hour at room temperature.

### *Immunohistochemistry*

Tissue punches were blocked in 10% Donkey-serum with 0.01% Sodium Azide and 0.25% Triton X-100 for 1-1.5 hours at room temperature then incubated in primary antibodies for 2-3 days at 4°C. Following primary antibody incubation, tissue was washed 4-5 times in 1xPBS for 20 minutes each and incubated in secondary antibodies overnight at 4°C. Tissue was

then washed 4-5 times in 1xPBS for 20 minutes each and incubated in a lectin stain, wheat germ agglutinin conjugated to Atto-488, overnight at 4°C to label cytoarchitecture.

### *Resin polymerization and ultrasectioning*

Following WGA staining, tissue was washed in 1xPBS 3 times for 20 minutes and post-fixed in 3% paraformaldehyde / 0.1% glutaraldehyde in 1xPBS for 2-3 hours at room temperature. Tissue was then wash one last time 2-3 times in 1xPBS for 20 minutes each, followed by graded ethanol dehydration series, 50%, 75%, 95%, 100%, 100%, for 20 minutes each. Dehydrated tissue was then infiltrated with Ultrabed Epoxy Resin (EMS) in increasing ratios diluted in 100% ethanol (2:1 overnight, 1:1 for 2 hours, 100% resin twice for 2 hours). Upon embedment in BEEM capsules (EMS), blocks were cured in a 70°C oven for 16-18 hours.

### STORM Imaging

#### *STORM acquisition and analysis*

Samples were prepared for STORM imaging via exposing photoswitching sites by chemically etching the resin and sealing into a flow chamber filled with STORM imaging buffer. Etching was achieved by incubation in 10% sodium ethoxide (NaEtOH) for 5 minutes. Excess NaEtOH was rinsed with 95% ethanol to prevent precipitation. Fluorescent beads (540/560 and 715/755 mixture) in two different concentrations were spotted to

serve as fiducial markers for chromatic aberration and flat field illumination corrections. Once the coverglass was adhered to a microscope slide using double sided tape, a STORM imaging buffer consisting of 10% glucose, 17.5 $\mu$ M glucose oxidase, 708nM catalase, 10mM mercaptoethylamine, 10mM NaCl, and 200mM Tris was flowed in and sealed with epoxy.

Image acquisition was performed using a custom built TIRF system through an inverted Nikon Ti confocal stand with a Nikon 60x 1.4NA TIRF objective. The corresponding lasers used for excitation were 488nm, 561nm, 647nm, and 750nm lines with a 405nm laser for secondary activation of far red (Alexa 647 and DyLight 750P1) STORM probes. Images were collected on a Hamamatsu Orca Flash CMOS camera with an overall field size of 96x96 $\mu$ m.

Using a Python based open source automated image acquisition software (Zhuang Lab GitHub), samples were tiled using a 4x 0.9NA objective and to achieve relative spatial position, then further tiled at 60x magnification to identify ROIs for image acquisition. Once ROIs were established, conventional resolution images were taken at each selected ROI, followed by STORM acquisition. The length of STORM imaging in each channel varied based on the signal in each respective wavelength; 750 contained 7000-8000 frames, 647 contained 6000-7000 frames, 561 contained 8000 frames (samples containing WGA in the 561 channel did not have STORM data taken), 488 contained 8000-10000 frames.

STORM analysis was performed using the open source DAOSTORM algorithm to calculate the centroid positions of individual molecules<sup>49</sup>. The corresponding molecule list was transformed to correct for chromatic aberrations caused by the imaging objective and flat field illuminance aberrations by using the transformation maps generated by bead images. Volumetric reconstruction of sections was achieved by alignment of adjacent sections using the WGA channel. The alignment algorithms (Fiji Processes) used were initially, the Scale-Invariant Feature Transform (SIFT) rigid alignment<sup>70</sup>, followed by elastic block matching alignment<sup>71</sup>. While the algorithms were sourced matched on adjacent sections, the parameters for transformation were applied through the volumetric stack.

### *STORM Dyes*

Custom STORM secondary antibody dyes were conjugated with corresponding species specificity to primary antibody host species. Previously quantified high quality STORM reporter probes (Atto 488, Cy3B, Alexa 647, DyLight 750P1) along with an activator probe, Alexa 405, were incubated in 80 $\mu$ L of respective IgG antibody, 10 $\mu$ L sodium bicarbonate, 2.2 $\mu$ L respective reporter probe, and 1.3 $\mu$ L activator probe for 20 minutes in a light sealed container. The resultant conjugated antibodies are then purified using a NAP-5 Sephadex column (GE Healthcare).

### *Ultrasectioning*

Cured samples were trimmed and sectioned on a Leica UC7 ultramicrotome. Blocks were trimmed using a diamond trim tool from Diatome and sections collected using a JumboHisto diamond also from diatome. Ultrathin sections were collected at 70nm onto coverslips coated with 0.5% gelatin / 0.05% chromium potassium sulfate. Coverslips containing sections were dried on a hot plate at 60°C to bond sections to the coverslip.

### **Results**

To examine the role of activity in the synaptic development of ipRGC terminals in the SCN, we utilized STORM super-resolution microscopy techniques to observe and quantify the changes in synaptic structure between wild-type and double Knock-Out conditions. In order to produce littermate controls, mice were selectively bred to produce double homozygous Knock-Outs ( $Opn4^{cre/cre} / PACAP^{fl/fl}$ ) and double heterozygous ( $Opn4^{cre/+} / PACAP^{fl/+}$ ) functional wild-type offspring with equal proportion. Following tissue immunostaining and polymerization into resin, samples were sectioned at 70nm on an ultramicrotome for a total of 7-10 $\mu$ m in depth. To control for depth variability in SCN cytoarchitecture, only sections from the central-most depth of the SCN were analyzed.

Once the raw STORM data was processed and fit based on the localized PSF, prospective synaptic clusters were identified by size and intensity. Each synaptic marker was able to be split into distinct populations in this manner and the identified clusters were able to be manually selected for further processing. To ensure the quantification of ipRGC terminals, only clusters paired within a 140 pixel shell between all synaptic markers were quantified.

A challenge in the processing of fitted STORM images was the presence of somatic signal (Fig. 4a). To counteract the non-synaptic background these clusters produced, we first created a filter to exclude signal within the soma based off of the collected conventional image (Fig. 4b). Additionally, previous STORM synaptic processing has used a watershed analysis to isolate connected structures to define a potential synaptic cluster. In the case of labeled synapses within the SCN, watershed artifacts caused erroneous splitting of synaptic clusters into 2 or more separate components, therefore altering the resultant quantifiable metrics of paired synapses.

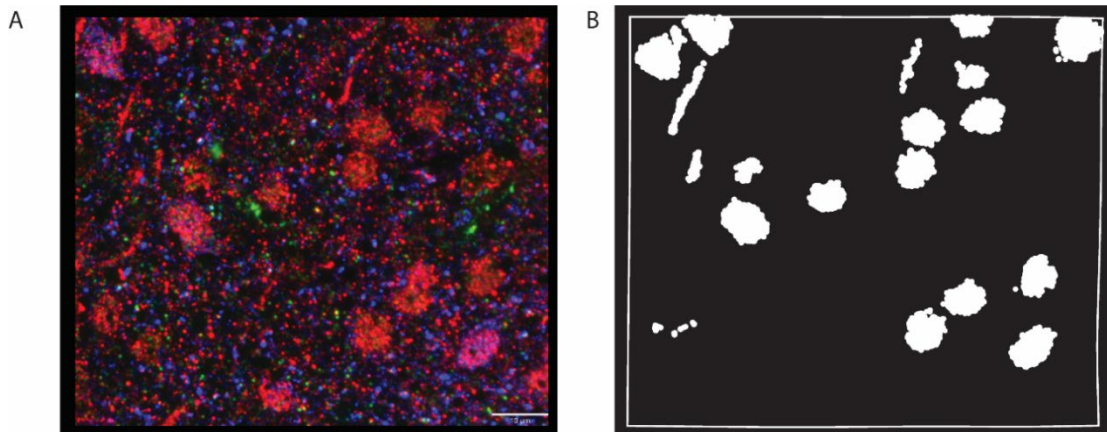


Figure 4. **Computational filtering of large somatic background noise**  
Computationally derived soma filters were calculated based on conventional images (A) in the specified color channel with the most somatic signal interference. Resulting filters (B) were applied to the image volume on a section by section basis, thereby occluding erroneous cluster identifications. Scale bar: 10 $\mu$ m

The three metrics chosen to quantify synaptic structure were the overall number of paired clusters, the size in nm<sup>3</sup>, and the intensity of the label associated with those clusters. In wild-type animals we would expect to see an inverse relationship between the number of clusters and the size of those clusters throughout development, conforming to the notion of Hebbian-based remodeling (Fig. 5). That being, as synapses mature with the input of coordinated activity, structure and strength of the synapse increases while decreasing axonal branching leading to fewer overall synapses. Finally, a unique feature of STORM imaging is the ability to provide information on the density of labeled protein by measuring the intensity profile of clusters.

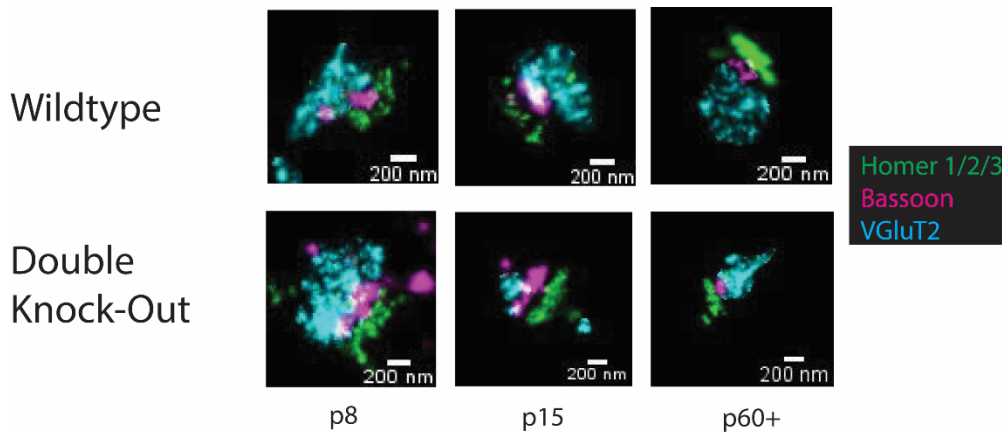
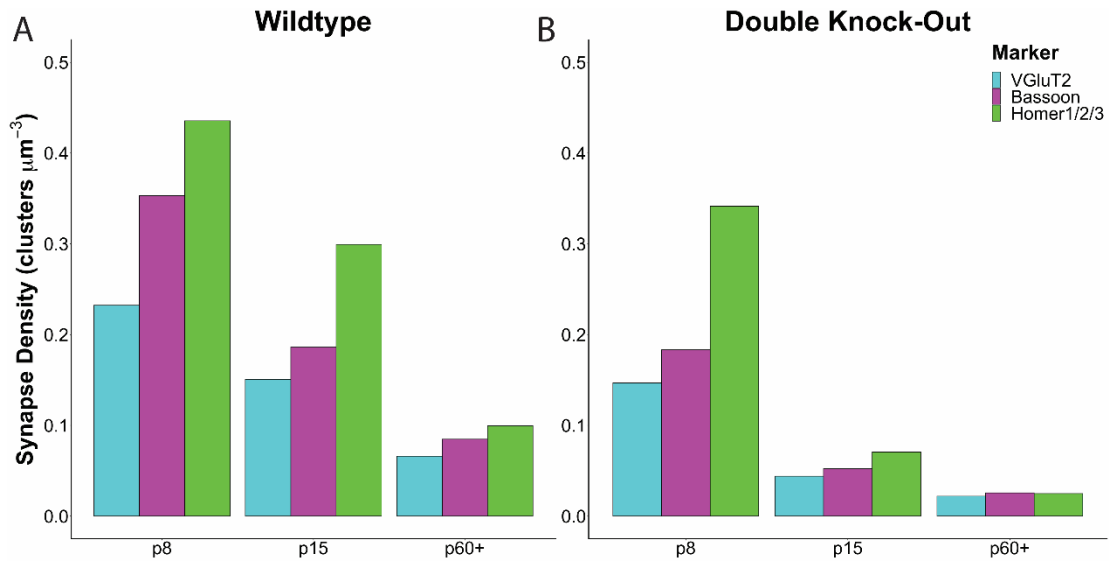


Figure 5. **STORM Imaging of Wildtype and Double Knock-Out Synapses**  
 Six example synapses across activity manipulation (Wildtype and double Knock-Out) across development. Paired synaptic clusters of Bassoon (green), Homer 1/2/3 (red), and VGLuT2 (magenta) are then quantified.

The effect of activity on overall synaptic density is clear, being markedly less in double Knock-Out conditions. The synaptic density of all clusters was reduced by an average of 35% in double Knock-Out conditions at p8, 73% at p15, and 70% in mature animals (Fig. 6a,b). As glutamate is the main neurotransmitter in ipRGCs, one would hypothesize the rush of photic activity at eye-opening in a photic activity deprived synapse would increase the cluster density of VGLuT2. The reduction in cluster density in mature double knock-out animals was consistent with expected results, having the lowest cluster density across development and condition. Overall, synapse density in wild-type animals followed Hebbian remodeling, decreasing in number throughout development as synapses mature. Double knock-out animals across development presented fewer synaptic clusters and decreased with age compared to wildtype animals.



**Figure 6. Synaptic Density per Marker Across Development**

Synaptic density was calculated by quantifying the total synaptic cluster count divided by the total volume of the imaged region. A) Wildtype developmental effect on synaptic density. B) Activity-perturbed (double Knock-Out) developmental effect on synaptic density. Density counts by marker are consistent with rendered images: Bassoon (green), Homer 1/2/3 (red), VGLuT2 (magenta).

Quantifying the volume of synaptic markers in response to activity perturbations again showed a positive Hebbian-based trend. In wild type animals the volume of synaptic markers increases with age, with the vesicular pool associate with VGLuT2 being the largest volume (Fig. 7a). Unlike the decrease in cluster density seen in double knock-out animals, the volume of VGLuT2 clusters still increases throughout development, albeit at a 48%, 55%, and 58% reduction for p8, p15, and p60+, respectively, compared to wild type (Fig. 7b). The continued increase in size can reflect the attempt to signal normally utilizing outer photoreceptor input.

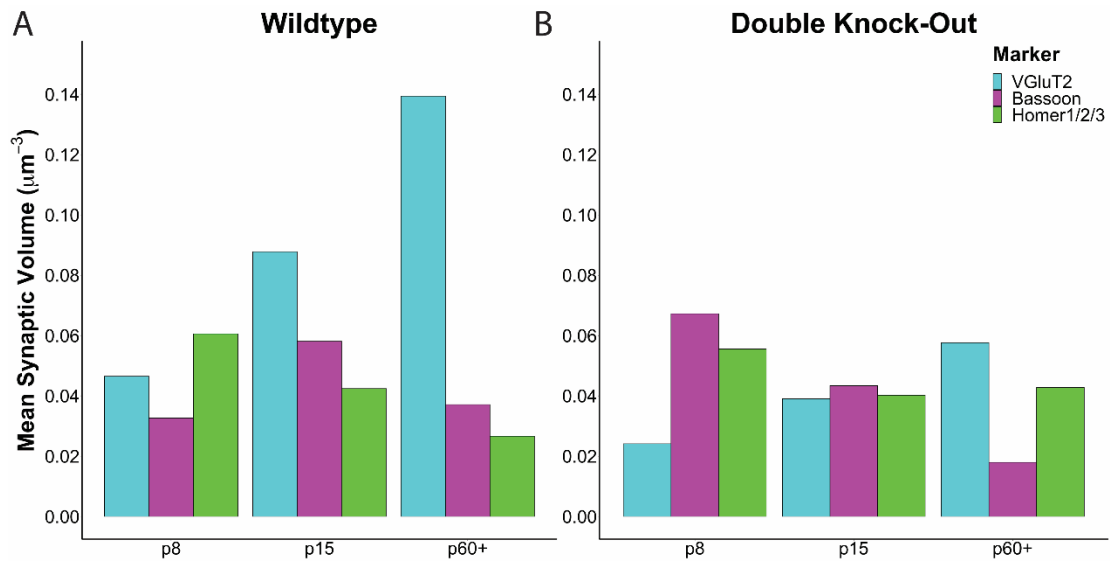


**Figure 7. Mean Synaptic Cluster Volume per Marker Across Development**  
 Mean synaptic cluster volume was calculated across development for each synaptic marker. A) Distribution of mean volume across development in wildtype animals. B) Distribution of mean volume across development in activity-manipulated double Knock-Out animals.

As STORM imaging is able to localize individual molecules, the resulting intensity within an image can provide information on the density of labeled molecules within the imaging field. Interestingly, the trend of intensity per condition is consistent across development for both wildtype and double Knock-Out conditions compared to area distributions (Fig. 8a,b). Interestingly, the intensity profile of synaptic proteins between Wildtype and Knock-Out conditions is similar (Fig. 8b). Additionally, the intensity profiles of VGlut2 match the developmental changes in synaptic area distributions.

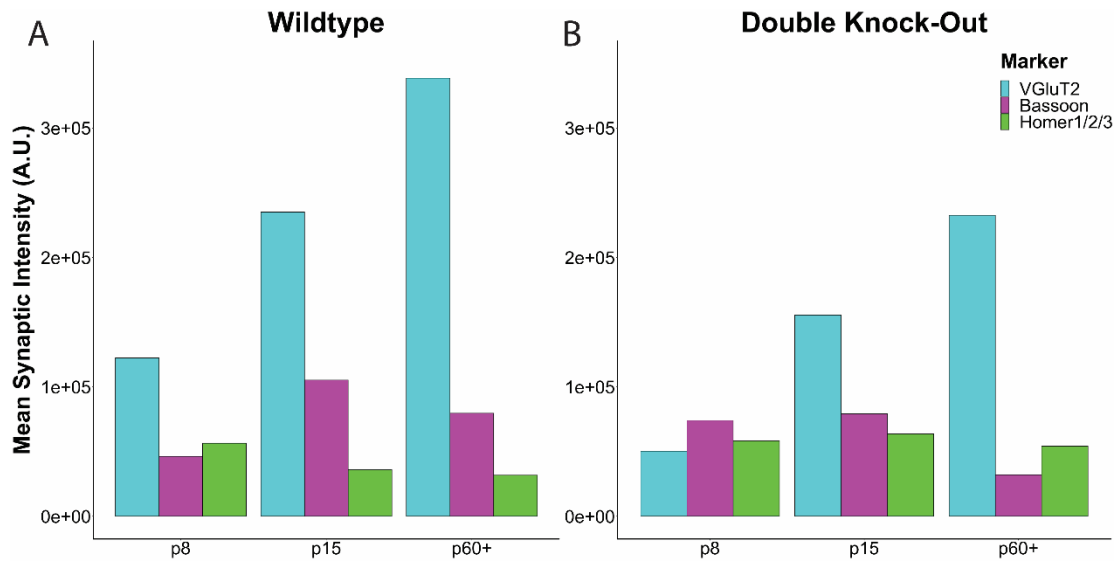


**Figure 8. Mean Synaptic Intensity per Marker Across Development**

The mean synaptic intensity per cluster volume was calculated by dividing the total intensity per cluster by cluster volume and averaged across all clusters. A) Distribution of mean intensity per cluster volume across development in wildtype animals. B) Distribution of mean intensity per cluster volume across development in activity-manipulated double Knock-Out animals.

These results suggest the reduction in photic activity from melanopsin associated signaling is sufficient to reduce the synaptic structure and VGLuT2 associated vesicle pools (Fig. 9). Additionally, despite the lack of melanopsin associated photic activity, Hebbian-based remodeling is still maintained in double knock-out animals as evidenced by the decrease in synaptic density while increasing in synaptic size (area). This suggests maintained synaptic pruning and refinement of the circadian circuit despite activity manipulations.

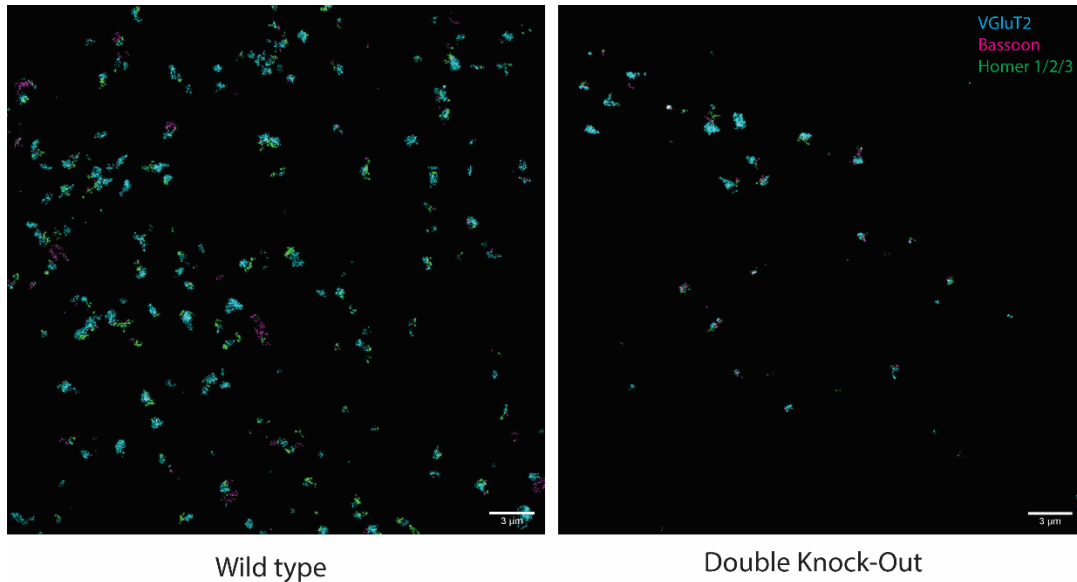


Figure 9. **Volumetric Comparison of Synapses in the SCN**  
 Maximum intensity projections of 10 sections (700nm) in adult SCN demonstrating the loss of synapse density and size between wild type and double knock-out conditions.

### **Discussion**

This work is the one of if not the first studies of activity-dependent structural changes in the SCN using super-resolution imaging. The trends we see in this study suggests the activity output of ipRGC specific signaling and its effect on synaptic structure in the SCN is highly correlated. Through the elimination of both unique signaling aspects of ipRGCs, melanopsin and PACAP, we were able to show a trend of reduced synaptic density and synapse size across development. This was particularly noticeable in VGlut2 clusters, most likely reflecting the lack of melanopsin associated glutamatergic drive. We are able to see a trend of decreasing number of identified paired synaptic structures through development as expected. However, the trend of synaptic protein mean size increasing across

development in the dKO condition is similar compared to wild type animals. It is known that light activity from rods and cones is sufficient to drive circadian rhythmicity in normal lighting conditions, however, lacks the ability to shift the phase of photoentrainment<sup>19,140</sup>. Therefore, further analysis and biological replicates could support the notion that this activity is sufficient to maintain synaptic size and suggest the main driver of circadian photoentrainment is the ability of ipRGCs to maintain large VGluT2 cluster pools in order to secrete glutamate.

The synaptic specializations of ipRGC neurons in the SCN can further be expanded by individual manipulation of signaling activity. Comparison of melanopsin knock-out, PACAP knock-out, and double-knock out conditions can reveal the relative contributions of activity to synaptic structure. Melanopsin associated glutamatergic signaling has shown to induce a transient response in circadian entrainment and the PLR, whereas PACAP signals for a sustained response<sup>69,97,141</sup>. STORM imaging of receptor content (NMDA, AMPA, or PACAP receptors) at the post-synaptic density can further inform changes in structural plasticity as it relates to function. As these glutamatergic and PACAPergic receptors are what allows for calcium influx and therefore proper entrainment signaling, a lower density of these receptors would infer alterations in functional signaling to retinorecipient neurons in the SCN. With the decrease in VGluT2 clusters associated with melanopsin knock-out and genetic ablation of PACAP signaling, we would expect the resultant physiological strength of these synapses to also be decreased. As

prior work on synaptic plasticity has shown long term potentiation being dependent on AMPA receptor addition to the post-synaptic density, it would be expected to see a reduction in AMPA current and receptor content in these double knock-out animals<sup>130,131,142–144</sup>. Electrophysiological recordings of retinorecipient neurons in the SCN can provide evidence the functional changes in synaptic transmission associated with the structural changes we see here.

Recent work from the lab of Satchidananda Panda has conducted a careful electron microscopical analysis of ipRGC terminals in the SCN and other brain regions that ipRGCs target. Their ability to quantify synaptic structures in a volumetric manner was through the use of a genetically encoded electron microscopy tag<sup>53</sup>. The resolution capability of electron microscopy allowed the annotation and quantification of ipRGC synapses within the SCN. A fascinating observation and subsequent quantification found approximately 10% of randomly selected dendrites within the volume were dendrodendritic synapses. These dendrodendritic synapses are characterized by a lack of post-synaptic densities and are thought to be associated with inhibitory, GABAergic neurons. The relative proportion of dendrodendritic ipRGC synaptic connections to monosynaptic connections suggested a high preference of ipRGCs to synapse onto these coupled neurons<sup>53</sup>. Potential evidence of these dendrodendritic synapses has been observed in wild type and double knock-out animals, however additional synapse pairing code structures must be further developed for accurate

quantification of these occurrences and therefore cannot be conclusively classified as dendrodendritic synapses. Quantification of ipRGC connections and their proximity to dendrodendritic synapses in response to activity manipulations can shed light on how local SCN neuron coupling may be altered.

Activity-dependent changes in synaptic structure and plasticity have been a hallmark of development and learning as well as disease<sup>22,108,126,145</sup>. Through the quantification of structural changes in the SCN in response to activity perturbations, we can aim to more fully understand the pathology and potential treatment methods linked to circadian disorders.

### **Thesis Discussion**

The presence or absence of environmental light controlling the circadian system is communicated to the Suprachiasmatic Nucleus (SCN) through the unique retinal ganglion cell, the intrinsically photosensitive retinal ganglion cell (ipRGC)<sup>19</sup>. Light is detected in ipRGCs through the invertebrate-like opsin, melanopsin, and drives an excitatory signal releasing glutamate and Pituitary Adenylate Cyclase Activating Peptide (PACAP) onto retinorecipient cells in the SCN<sup>96,97,141</sup>. The resulting excitatory signal from ipRGCs causes the cAMP Response Element Binding (CREB) induction of circadian gene expression (*Per* genes), thus signaling the onset of light and entraining the circadian rhythm to this cue<sup>6,90</sup>. The proper control and

synchrony of the circadian rhythm to environmental light has been shown to be dependent on ipRGC connection to the SCN and light signal from at least rods and cones<sup>3,146,147</sup>. Previous studies have explored the effect of genetically ablated ipRGC activity from melanopsin and PACAP signal on Pupillary Light Reflex (PLR); however, the extent to which this activity manipulation affects circadian photoentrainment and the synaptic structure of ipRGC-SCN connections has yet to be determined<sup>29,148</sup>.

Our analysis of synaptic markers in the SCN is the first characterization of quality STORM labeling for the visualization of synaptic proteins, including adequate molecular localization and labeling density. The pre- and post-synaptic markers of Bassoon and Homer respectively have been shown to undergo activity-dependent restructuring<sup>73,74,77</sup>. Additionally, changes in VGluT2 clustering served as an accurate marker of glutamatergic activity being relayed to post-synaptic neurons. The SCN primarily coordinates its interneuronal signaling through GABA neurotransmission to couple rhythm generation throughout the nucleus<sup>81,149–151</sup>. Recent evidence has also shown evidence of GABA signaling from a subset of ipRGCs to retinorecipient neurons in the SCN<sup>27</sup>. Therefore, further characterization of inhibitory synaptic markers could expand the understanding of synaptic structural change in response to activity manipulations. This can be done by immunolabeling with inhibitory scaffolding proteins such as gephyrin and/or inhibitory receptors such as GABA and Glycine subunits. The relative position of ipRGC GABAergic synapses on retinorecipient neurons and the effect of

activity manipulations on the structure of these synapses can also be gleaned from this type of study.

The effects of activity manipulations through studies of blockade and overexpression of activity have been shown to either reduce or increase activity-dependent synaptogenesis, respectively<sup>42,43,152,153</sup>. Through the genetic ablation of melanopsin associated glutamatergic signaling and PACAP signaling in order to manipulate activity patterns of the ipRGC-SCN circuit, we asked the question of how the reduction in activity would affect the synaptic structure throughout development. As prior work has shown the ability of mice to retain proper circadian entrainment after ablation of melanopsin but not phase shifting, we hypothesized the synaptic structure as a result of ipRGC activity manipulations would be reduced but not completely absent<sup>29,154</sup>. Remaining activity due to spontaneous retinal waves and input from rods and cones after eye opening would justify the observation of synapses throughout development<sup>106,117,155,156</sup>. After calculating paired structures and identifying an ipRGC-SCN synapse (paired VGluT2, pre-, and post-synaptic structures), we quantified the size, intensity per cluster area, and overall synapse density for each synaptic marker. The finding of similar developmental trends in VGluT2 cluster volume in activity-manipulated animals suggests photoentrainment is still active under rod and cone signaling control. Further experimentation can be done to assess the change in receptor content on SCN neurons to aid in answering questions of physiological change in these synapses. Of interest would be to quantify the

expression of the PAC1 receptor corresponding to PACAP signaling in response to activity manipulation. As previously discussed, PACAP modulates the glutamatergic signal from ipRGCs through the PAC1 receptor, increasing AMPA calcium signaling and acting as a gain control mechanism during the subjective night<sup>26,141,157</sup>. Therefore, it can be hypothesized that without PACAPergic signaling from ipRGCs, there would be a loss of the PAC1 receptor on retinorecipient neurons, and thus a lack of glutamatergic gain control. STORM imaging of the PAC1 receptor, as well as NMDA and AMPA receptors could tell us not only the position of these receptors on the PSD, but their change in expression in response to limited ipRGC activity. Understanding the activity-dependent changes in synapses signaling photoentrainment in the SCN can provide insight into the many altered circadian associated behaviors and disorders. It has been reported that >80% of primate protein-encoding genes follow a circadian expression pattern across central and peripheral tissues<sup>40,158</sup>. Thus, the precise control of circadian behaviors, and the consequences of altered behavior, become apparent across the body system, affecting locomotion, appetite, mood, and cognitive state<sup>4,35,91</sup>. Altered circadian function has been reported as a potential cause for many different disorders such as Seasonal Affective Disorder (SAD), onset of diabetes, cardiovascular disease, and behaviors associated with Parkinson's and Alzheimer's disease<sup>34,36-39,93</sup>. Therefore, altered synaptic structure of ipRGC input to the SCN and its ability to entrain the circadian system can have profound effects on the health and behavior of

the body. Through the understanding of how changes in activity affect the synaptic structure and signaling entraining the circadian clock, we can hope to understand the potential causes for circadian linked disorders.

## **Bibliography**

1. Daan, S. Colin Pittendrigh, Jurgen Aschoff, and the natural entrainment of circadian systems. *J. Biol. Rhythms* **15**, 195–207 (2000).
2. Aschoff, J. & Background, B. Circadian Rhythms in Man. *Science (80-. )*. **148**, 1427–1432 (1942).
3. Rupp, A. C. *et al.* Distinct ipRGC subpopulations mediate light's acute and circadian effects on body temperature and sleep. *Elife* **8**, (2019).
4. Fernandez, D. C. *et al.* Light Affects Mood and Learning through Distinct Retina-Brain Pathways. *Cell* **175**, 71-84.e18 (2018).
5. Sargent, M. L., Briggs, W. R. & Woodward, D. O. Circadian Nature of a Rhythm Expressed by an Invertaseless Strain of *Neurospora crassa*. *Plant Physiol.* **41**, 1343–1349 (2008).
6. Hastings, M. H., Maywood, E. S. & Brancaccio, M. Generation of circadian rhythms in the suprachiasmatic nucleus. *Nat. Rev. Neurosci.* **1** (2018). doi:10.1038/s41583-018-0026-z
7. Dibner, C., Schibler, U. & Albrecht, U. *The Mammalian Circadian Timing System: Organization and Coordination of Central and Peripheral Clocks. Annual Review of Physiology* **72**, (2010).
8. Czeisler, C. A. *et al.* Stability, precision, and near-24-hour period of the human circadian pacemaker. *Science (80-. )*. **284**, 2177–2181 (1999).
9. Welsh, D. K., Diomedes E. Logothetis, Meister, M. & Steven M. Reppert. Individual Neurons Dissociated from Rat Suprachiasmatic Nucleus Express Independently Phased Circadian Firing Rhythms.

- Neuron* **14**, 697–706 (1995).
10. Konopka, R. J. & Benzer, S. Clock Mutants of *Drosophila melanogaster*. *Proc. Natl. Acad. Sci.* **68**, 2112–2116 (2006).
  11. Konopka, R. J. Genetics of biological rhythms in *Drosophila*. *Annu. Rev. Genet.* **21**, 227–236 (1987).
  12. Allada, R., White, N. E., So, W. V., Hall, J. C. & Rosbash, M. A mutant *Drosophila* homolog of mammalian clock disrupts circadian rhythms and transcription of period and timeless. *Cell* **93**, 791–804 (1998).
  13. Nuzzo, R. Profile of Jeffrey C. Hall. *Proc. Natl. Acad. Sci.* **102**, 16547–16549 (2005).
  14. Edwards, M. D., Maywood, E. S., Hastings, M. H., Brancaccio, M. & Chesham, J. E. Rhythmic expression of cryptochrome induces the circadian clock of arrhythmic suprachiasmatic nuclei through arginine vasopressin signaling. *Proc. Natl. Acad. Sci.* **113**, 2732–2737 (2016).
  15. Young, M. W. & Kay, S. A. Time zones: A comparative genetics of circadian clocks. *Nat. Rev. Genet.* **2**, 702–715 (2001).
  16. Welsh, D. K., Takahashi, J. S. & Kay, S. A. Suprachiasmatic Nucleus: Cell Autonomy and Network Properties. *Annu. Rev. Physiol.* **72**, 551–577 (2010).
  17. Do, M. T. H. Melanopsin and the Intrinsically Photosensitive Retinal Ganglion Cells: Biophysics to Behavior. *Neuron* **104**, 205–226 (2019).
  18. Lucas, R. J. *et al.* Measuring and using light in the melanopsin age. *Trends Neurosci.* **37**, 1–9 (2014).

19. Hattar, S., Liao, H., Takao, M., Berson, D. & Yau, K. Melanopsin-Containing Retinal Ganglion Cells: Architecture, Projections, and Intrinsic Photosensitivity. *Science (80-. )*. **295**, 1065–1070 (2002).
20. Berson, D. M., Dunn, F. A. & Takao, M. Phototransduction by Retinal Ganglion Cells That Set the Circadian Clock. *Science (80-. )*. **395**, 224 (2002).
21. Graham, D. M. *et al.* Melanopsin ganglion cells use a membrane-associated rhabdomic phototransduction cascade. *J. Neurophysiol.* **99**, 2522–2532 (2008).
22. Gompf, H. S., Fuller, P. M., Hattar, S., Saper, C. B. & Lu, J. Impaired circadian photosensitivity in mice lacking glutamate transmission from retinal melanopsin cells. *J. Biol. Rhythms* **30**, 35–41 (2015).
23. Berson, D. M. Phototransduction in ganglion-cell photoreceptors. *Pflugers Arch. Eur. J. Physiol.* **454**, 849–855 (2007).
24. Hannibal, J., Møller, M., Ottersen, O. P. & Fahrenkrug, J. PACAP and glutamate are co-stored in the retinohypothalamic tract. *J. Comp. Neurol.* **418**, 147–155 (2000).
25. Lindberg, P. T. *et al.* Pituitary Adenylate Cyclase-Activating Peptide (PACAP)-Glutamate Co-transmission Drives Circadian Phase-Advancing Responses to Intrinsically Photosensitive Retinal Ganglion Cell Projections by Suprachiasmatic Nucleus. *Front. Neurosci.* **13**, 1–13 (2019).
26. Chen, D., Buchanan, G. F., Ding, J. M., Hannibal, J. & Gillette, M. U.

- Pituitary adenylyl cyclase-activating peptide: A pivotal modulator of glutamatergic regulation of the suprachiasmatic circadian clock. *Proc. Natl. Acad. Sci. U. S. A.* **96**, 13468–13473 (1999).
27. Sonoda, T. *et al.* A noncanonical inhibitory circuit dampens behavioral sensitivity to light. *Science (80-. )*. **368**, 527–531 (2020).
  28. Schmidt, T. M., Chen, S. K. & Hattar, S. Intrinsically photosensitive retinal ganglion cells: Many subtypes, diverse functions. *Trends Neurosci.* **34**, 572–580 (2011).
  29. Chen, S. K., Badea, T. C. & Hattar, S. Photoentrainment and pupillary light reflex are mediated by distinct populations of ipRGCs. *Nature* **476**, 92–96 (2011).
  30. Keenan, W. T. *et al.* A visual circuit uses complementary mechanisms to support transient and sustained pupil constriction. *Elife* **5**, 1–23 (2016).
  31. Sekaran, S. *et al.* Melanopsin-dependent photoreception provides earliest light detection in the mammalian retina. *Curr. Biol.* **15**, 1099–1107 (2005).
  32. Ramkisoensing, A. & Meijer, J. H. Synchronization of biological clock neurons by light and peripheral feedback systems promotes circadian rhythms and health. *Front. Neurol.* **6**, 1–16 (2015).
  33. Abrahamson, E. E. & Moore, R. Y. Suprachiasmatic nucleus in the mouse: Retinal innervation, intrinsic organization and efferent projections. *Brain Res.* **916**, 172–191 (2001).

34. Richardson, M. E. S., Parkins, S., Kaneza, I. & Dauphin, A. C. Jet Lag Recovery and Memory Functions Are Correlated with Direct Light Effects on Locomotion. *J. Biol. Rhythms* 1–10 (2020).  
doi:10.1177/0748730420947589
35. Abrahamson, E. E. & Moore, R. Y. Lesions of suprachiasmatic nucleus efferents selectively affect rest-activity rhythm. *Mol. Cell. Endocrinol.* **252**, 46–56 (2006).
36. Ortuño-Lizarán, I. *et al.* Degeneration of human photosensitive retinal ganglion cells may explain sleep and circadian rhythms disorders in Parkinson's disease. *Acta Neuropathol. Commun.* **6**, 1–10 (2018).
37. La Morgia, C. *et al.* Melanopsin retinal ganglion cell loss in Alzheimer disease. *Ann. Neurol.* **79**, 90–109 (2016).
38. White, C. Seasonal affective disorder. *5-Minute Clin. Consult Stand. 2016 Twenty Fourth Ed.* 1037–1041 (2015).
39. Todd, W. D. Potential Pathways for Circadian Dysfunction and Sundowning-Related Behavioral Aggression in Alzheimer's Disease and Related Dementias. *Front. Neurosci.* **14**, 1–14 (2020).
40. Zhang, R., Lahens, N. F., Ballance, H. I., Hughes, M. E. & Hogenesch, J. B. A circadian gene expression atlas in mammals: Implications for biology and medicine. *Proc. Natl. Acad. Sci. U. S. A.* **111**, 16219–16224 (2014).
41. Poncer, J. C. & Malinow, R. Postsynaptic conversion of silent synapses during LTP affects synaptic gain and transmission dynamics. *Nat.*

- Neurosci.* **4**, 989–996 (2001).
42. Murthy, V. N., Schikorski, T., Stevens, C. F. & Zhu, Y. Inactivity produces increases in neurotransmitter release and synapse size. *Neuron* **32**, 673–682 (2001).
43. Uesaka, N., Hirai, S., Maruyama, T., Ruthazer, E. S. & Yamamoto, N. Activity dependence of cortical axon branch formation: A morphological and electrophysiological study using organotypic slice cultures. *J. Neurosci.* **25**, 1–9 (2005).
44. Kutsarova, E., Munz, M. & Ruthazer, E. S. Rules for shaping neural connections in the developing brain. *Front. Neural Circuits* **10**, 1–16 (2017).
45. Chalupa, L. M. A reassessment of the role of activity in the formation of eye-specific retinogeniculate projections. *Brain Res. Rev.* **55**, (2007).
46. Leamey, C. A., Wart, A. Van & Sur, M. Intrinsic patterning and experience-dependent mechanisms that generate eye-specific projections and binocular circuits in the visual pathway. *Curr. Opin. Neurobiol.* (2009). doi:10.1016/j.conb.2009.05.006
47. Penn, A. A., Riquelme, P. A., Feller, M. B. & Shatz, C. J. Competition in retinogeniculate patterning driven by spontaneous activity. *Science* (80-). **279**, 2108–2112 (1998).
48. Hess, S. T., Girirajan, T. P. K. & Mason, M. D. Ultra-high resolution imaging by fluorescence photoactivation localization microscopy. *Biophys. J.* **91**, 4258–4272 (2006).

49. Bates, M., Jones, S. A. & Zhuang, X. Stochastic optical reconstruction microscopy (STORM): A method for superresolution fluorescence imaging. *Cold Spring Harb. Protoc.* **8**, 498–520 (2013).
50. Betzig, E. *et al.* Imaging Intracellular Fluorescent Proteins at Nanometer Resolution. *Sci. (Washington, DC, United States)* **313**, 1642–1645 (2006).
51. SW, H. & Wichmann, J. Breaking the diffraction resolution limit by stimulated emission: stimulated-emission-depletion fluorescence microscopy. *Opt. Lett.* **19**, 780–782 (1994).
52. Morin, L. P. Neuroanatomy of the extended circadian rhythm system. *Exp. Neurol.* **243**, 4–20 (2013).
53. Kim, K.-Y. *et al.* Synaptic Specializations of Melanopsin-Retinal Ganglion Cells in Multiple Brain Regions Revealed by Genetic Label for Light and Electron Microscopy. *Cell Rep.* **29**, 628-644.e6 (2019).
54. Irwin, R. P. & Allen, C. N. Calcium response to retinohypothalamic tract synaptic transmission in suprachiasmatic nucleus neurons. *J. Neurosci.* **27**, 11748–11757 (2007).
55. Huang, B., Babcock, H. & Zhuang, X. Breaking the diffraction barrier: Super-resolution imaging of cells. *Cell* **143**, 1047–1058 (2010).
56. Huang, B., Bates, M. & Zhuang, X. Super-Resolution Fluorescence Microscopy. *Annu. Rev. Biochem.* **78**, 993–1016 (2009).
57. Maglione, M. & Sigrist, S. J. Seeing the forest tree by tree: super-resolution light microscopy meets the neurosciences. *Nat. Neurosci.* **16**,

- 790–797 (2013).
58. Gustafsson, M. G. L. Nonlinear structured-illumination microscopy: Wide-field fluorescence imaging with theoretically unlimited resolution. *Proc. Natl. Acad. Sci. U. S. A.* **102**, 13081–13086 (2005).
  59. Dempsey, G. T., Wang, W. & Zhuang, X. *Fluorescence Imaging at Sub-Diffraction-Limit Resolution with Stochastic Optical Reconstruction Microscopy*. (2009). doi:10.1007/978-0-387-76497-9
  60. Bates, M., Huang, B., Dempsey, G. T. & Zhuang, X. Multicolor super-resolution imaging with photo-switchable fluorescent probes. *Science (80-. )*. **317**, 1749–1753 (2007).
  61. Rust, M. J., Bates, M. & Zhuang, X. Sub-diffraction-limit imaging by stochastic optical reconstruction microscopy (STORM). *Nat. Methods* **3**, 793–795 (2006).
  62. Dempsey, G. T., Vaughan, J. C., Chen, K. H., Bates, M. & Zhuang, X. Evaluation of fluorophores for optimal performance in localization-based super-resolution imaging. *Nat. Methods* **8**, 1027–1040 (2011).
  63. Dempsey, G. T. *et al.* Photoswitching mechanism of cyanine dyes. *J. Am. Chem. Soc.* **131**, 18192–18193 (2009).
  64. Bates, M., Huang, B., Dempsey, G. T., Zhuang, X. & Dempsey, T. Multicolor Super-Resolution Imaging with Photo-Switchable Probes Fluorescent. *Science (80-. )*. **317**, 1749–1753 (2007).
  65. Shroff, H., Galbraith, C. G., Galbraith, J. A. & Betzig, E. Live-cell photoactivated localization microscopy of nanoscale adhesion

- dynamics. *Nat. Methods* **5**, 417–423 (2008).
66. Axelrod, D. Total Internal Reflection Fluorescence Microscopy. *Encycl. Cell Biol.* **2**, 62–69 (2016).
  67. Girardet, C. *et al.* Daily changes in synaptic innervation of VIP neurons in the rat suprachiasmatic nucleus: Contribution of glutamatergic afferents. *Eur. J. Neurosci.* **31**, 359–370 (2010).
  68. Ecker, J. L. *et al.* Melanopsin-expressing retinal ganglion-cell photoreceptors: Cellular diversity and role in pattern vision. *Neuron* **67**, 49–60 (2010).
  69. Keenan, W. T. *et al.* A visual circuit uses complementary mechanisms to support transient and sustained pupil constriction. *Elife* **5**, 1–23 (2016).
  70. Lowe, D. G. Distinctive image features from scale-invariant keypoints. *Int. J. Comput. Vis.* **60**, 91–110 (2004).
  71. Saalfeld, S., Fetter, R., Cardona, A. & Tomancak, P. Elastic volume reconstruction from series of ultra-thin microscopy sections - SUPP. *Nat. Methods* **9**, 717–720 (2012).
  72. Lucas, R. J., Freedman, M. S., Muñoz, M., Garcia-Fernández, J. M. & Foster, R. G. Regulation of the mammalian pineal by non-rod, non-cone, ocular photoreceptors. *Science (80-. )*. **284**, 505–507 (1999).
  73. Shiraishi-Yamaguchi, Y. & Furuichi, T. The Homer family proteins. *Genome Biol.* **8**, 1–12 (2007).
  74. Gundelfinger, E. D., Reissner, C. & Garner, C. C. Role of Bassoon and

- Piccolo in Assembly and Molecular Organization of the Active Zone. *Front. Synaptic Neurosci.* **7**, (2016).
75. Glebov, O. O., Cox, S., Humphreys, L. & Burrone, J. Neuronal activity controls transsynaptic geometry. *Sci. Rep.* **6**, 1–11 (2016).
76. Bottai, D. *et al.* Synaptic activity-induced conversion of intronic to exonic sequence in Homer 1 immediate early gene expression. *J. Neurosci.* **22**, 167–175 (2002).
77. Sala, C. *et al.* Inhibition of dendritic spine morphogenesis and synaptic transmission by activity-inducible protein Homer1a. *J. Neurosci.* **23**, 6327–6337 (2003).
78. Tao-Cheng, J. H., Thein, S., Yang, Y., Reese, T. S. & Gallant, P. E. Homer is concentrated at the postsynaptic density and does not redistribute after acute synaptic stimulation. *Neuroscience* **266**, 80–90 (2014).
79. Dani, A., Huang, B., Bergan, J., Dulac, C. & Zhuang, X. Superresolution Imaging of Chemical Synapses in the Brain. *Neuron* **68**, 843–856 (2010).
80. Sigal, Y. M., Speer, C. M., Babcock, H. P. & Zhuang, X. Mapping Synaptic Input Fields of Neurons with Super-Resolution Imaging. *Cell* **163**, 493–505 (2015).
81. Albers, H. E. *et al.* The dynamics of GABA signaling: Revelations from the circadian pacemaker in the suprachiasmatic nucleus. *Front. Neuroendocrinol.* 35–82 (2017). doi:10.1016/j.yfrne.2016.11.003.The

82. Shigeoka, T. *et al.* Dynamic Axonal Translation in Developing and Mature Visual Circuits. *Cell* 181–192 (2016). doi:10.1016/j.cell.2016.05.029
83. Chozinski, T. J. *et al.* Expansion microscopy with conventional antibodies and fluorescent proteins. *Nat. Methods* **13**, 485–488 (2016).
84. Chen, F., Tillberg, P. W. & Boyden, E. S. Expansion microscopy. *Science (80-. )*. **347**, 543–548 (2015).
85. Wang, Y. *et al.* Rapid sequential in situ multiplexing with DNA-Exchange-Imaging in Neuronal Cells and Tissues. *Nano Lett.* acs.nanolett.7b02716 (2017). doi:10.1021/acs.nanolett.7b02716
86. Schnitzbauer, J., Strauss, M. T., Schlichthaerle, T., Schueder, F. & Jungmann, R. Super-resolution microscopy with DNA-PAINT. *Nat. Protoc.* **12**, 1198–1228 (2017).
87. Jungmann, R. *et al.* Multiplexed 3D cellular super-resolution imaging with DNA-PAINT and Exchange-PAINT. *Nat. Methods* **11**, 313–318 (2014).
88. Enoki, R. *et al.* Synchronous circadian voltage rhythms with asynchronous calcium rhythms in the suprachiasmatic nucleus. *Proc. Natl. Acad. Sci.* **114**, E2476–E2485 (2017).
89. Shan, Y. *et al.* Dual-Color Single-Cell Imaging of the Suprachiasmatic Nucleus Reveals a Circadian Role in Network Synchrony. *Neuron* 1–16 (2020). doi:10.1016/j.neuron.2020.07.012
90. Hastings, M. H., Brancaccio, M. & Maywood, E. S. Circadian

- pacemaking in cells and circuits of the suprachiasmatic nucleus. *J. Neuroendocrinol.* **26**, 2–10 (2014).
91. Lazzerini Ospri, L., Prusky, G. & Hattar, S. Mood, the Circadian System, and Melanopsin Retinal Ganglion Cells. *Annu. Rev. Neurosci.* **40**, 539–556 (2017).
  92. Hatori, M. & Panda, S. The emerging roles of melanopsin in behavioral adaptation to light. *Trends Mol. Med.* **16**, 435–446 (2010).
  93. An, K. *et al.* A circadian rhythm-gated subcortical pathway for nighttime-light-induced depressive-like behaviors in mice. *Nat. Neurosci.* **23**, (2020).
  94. Marcheva, B. *et al.* Disruption of the Clock Components CLOCK and BMAL1 Leads to Hypoinsulinemia and Diabetes. *Nature* **466**, 627–631 (2010).
  95. Lax, P., Ortuño-Lizarán, I., Maneu, V., Vidal-Sanz, M. & Cuenca, N. Photosensitive melanopsin-containing retinal ganglion cells in health and disease: Implications for circadian rhythms. *Int. J. Mol. Sci.* **20**, (2019).
  96. Graham, D. M. *et al.* Melanopsin ganglion cells use a membrane-associated rhabdomeric phototransduction cascade. *J. Neurophysiol.* **99**, 2522–2532 (2008).
  97. Do, M. T. H. & Yau, K. W. Intrinsically photosensitive retinal ganglion cells. *Physiol. Rev.* **90**, 1547–1581 (2010).
  98. Do, M. T. H. *et al.* Photon capture and signalling by melanopsin retinal

- ganglion cells. *Nature* **457**, 281–287 (2009).
99. Schmidt, T. M. *et al.* Melanopsin-Positive Intrinsically Photosensitive Retinal Ganglion Cells : From Form To Function. *J Neurosci* **31**, 16094–16101 (2012).
  100. Schmidt, T. M., Taniguchi, K. & Kofuji, P. Intrinsic and extrinsic light responses in melanopsin-expressing ganglion cells during mouse development. *J. Neurophysiol.* **100**, 371–384 (2008).
  101. Gillette, M. U. & Mitchell, J. W. Signaling in the suprachiasmatic nucleus: Selectively responsive and integrative. *Cell Tissue Res.* **309**, 99–107 (2002).
  102. Hannibal, J. *et al.* Pituitary Adenylate Cyclase-Activating Peptide (PACAP) in the Retinohypothalamic Tract: A Potential Daytime Regulator of the Biological Clock. *J. Neurosci.* **17**, 2637–2644 (1997).
  103. Collins, B. *et al.* Circadian VIPergic Neurons of the Suprachiasmatic Nuclei Sculpt the Sleep-Wake Cycle. *Neuron* 1–14 (2020).  
doi:10.1016/j.neuron.2020.08.001
  104. Jones, J. R., Simon, T., Lones, L. & Herzog, E. D. SCN VIP neurons are essential for normal light-mediated resetting of the circadian system. *J. Neurosci.* **38**, 7986–7995 (2018).
  105. Mazuski, C. *et al.* Entrainment of Circadian Rhythms Depends on Firing Rates and Neuropeptide Release of VIP SCN Neurons. *Neuron* 555–563 (2018).
  106. Firth, S. I., Wang, C. T. & Feller, M. B. Retinal waves: Mechanisms and

- function in visual system development. *Cell Calcium* **37**, 425–432 (2005).
107. Xu, H. ping *et al.* An Instructive Role for Patterned Spontaneous Retinal Activity in Mouse Visual Map Development. *Neuron* **70**, 1115–1127 (2011).
108. Butts, D. A., Kanold, P. O. & Shatz, C. J. A Burst-Based “ Hebbian ” Learning Rule at Retinogeniculate Synapses Links Retinal Waves to Activity-Dependent Refinement. *PLoS Biol.* **5**, (2007).
109. Iwai, L. & Kawasaki, H. MOLECULAR DEVELOPMENT OF THE LATERAL GENICULATE NUCLEUS IN THE ABSENCE OF RETINAL WAVES DURING THE TIME OF RETINAL AXON EYE-SPECIFIC SEGREGATION. *Neuroscience* **159**, 1326–1337 (2009).
110. Arroyo, D. A. & Feller, M. B. Spatiotemporal features of retinal waves instruct the wiring of the visual circuitry. *Front. Neural Circuits* **10**, 1–7 (2016).
111. Xu, H. P. *et al.* Retinal wave patterns are governed by mutual excitation among starburst amacrine cells and drive the refinement and maintenance of visual circuits. *J. Neurosci.* **36**, 3871–3886 (2016).
112. Burbridge, T. J. *et al.* Visual Circuit Development Requires Patterned Activity Mediated by Retinal Acetylcholine Receptors. *Neuron* **84**, 1049–1064 (2014).
113. Ford, K. J., Félix, A. L. & Feller, M. B. Cellular mechanisms underlying spatiotemporal features of cholinergic retinal waves. *J. Neurosci.* **32**,

- 850–863 (2012).
114. Bansal, A. *et al.* Mice Lacking Specific Nicotinic Acetylcholine Receptor Subunits Exhibit Dramatically Altered Spontaneous Activity Patterns and Reveal a Limited Role for Retinal Waves in Forming ON and OFF Circuits in the Inner Retina. *J. Neurosci.* **20**, 7672–7681 (2000).
  115. Feller, M. B. The role of nAChR-mediated spontaneous retinal activity in visual system development. *J. Neurobiol.* **53**, 556–567 (2002).
  116. Assali, A., Gaspar, P. & Rebsam, A. Activity dependent mechanisms of visual map formation - From retinal waves to molecular regulators. *Semin. Cell Dev. Biol.* **35**, 136–146 (2014).
  117. Wong, R. O. L. Retinal Waves and Visual System Development. *Annu. Rev. Neurosci.* **22**, 29–47 (1999).
  118. Stellwagen, D., Shatz, C. J., Feller, M. B. & Hughes, H. Dynamics of Retinal Waves Are Controlled by Cyclic AMP. *Neuron* **24**, 673–685 (1999).
  119. Ackman, J. B., Burbridge, T. J. & Crair, M. C. Retinal waves coordinate pattered activity throughout the developing visual system. *Nature* **490**, 219–225 (2012).
  120. Penn, A. A. Competition in Retinogeniculate Patterning Driven by Spontaneous Activity. *Science (80-. )*. **279**, 2108–2112 (1998).
  121. Sun, C., Speer, C. M., Wang, G., Chapman, B. & Chalupa, L. M. Epibatidine Application In Vitro Blocks Retinal Waves Without Silencing All Retinal Ganglion Cell Action Potentials in Developing Retina of the

- Mouse and Ferret. *J. Neurophysiol.* 3253–3263 (2008).  
doi:10.1152/jn.90303.2008.
122. Furman, M., Xu, H. & Crair, M. C. Competition driven by retinal waves promotes morphological and functional synaptic development of neurons in the superior colliculus. *J. Neurophysiol.* **110**, 1441–1454 (2019).
123. Hannibal, J. & Fahrenkrug, J. Melanopsin containing retinal ganglion cells are light responsive from birth. *Neuroreport* **15**, 2317–2320 (2004).
124. Verweij, J. *et al.* Light responses of melanopsin-expressing ganglion cells in the foetal mammalian retina. *bioRxiv* **7351**, (2019).
125. Lai, K. O. & Ip, N. Y. Structural plasticity of dendritic spines: The underlying mechanisms and its dysregulation in brain disorders. *Biochim. Biophys. Acta - Mol. Basis Dis.* **1832**, 2257–2263 (2013).
126. Huberman, A. D., Speer, C. M. & Chapman, B. Spontaneous Retinal Activity Mediates Development of Ocular Dominance Columns and Binocular Receptive Fields in V1. *Neuron* **52**, 247–254 (2006).
127. Chang, J. T., Whitney, D. & Fitzpatrick, D. Experience-Dependent Reorganization Drives Development of a Binocularly Unified Cortical Representation of Orientation. *Neuron* **107**, 338-350.e5 (2020).
128. Ruthazer, E. S. You're perfect, now change - Redefining the role of developmental plasticity. *Neuron* **45**, 825–828 (2005).
129. Inoue, Y., Udo, H., Inokuchi, K. & Sugiyama, H. Homer1a regulates the activity-induced remodeling of synaptic structures in cultured

- hippocampal neurons. *Neuroscience* **150**, 841–852 (2007).
130. Chen, X. *et al.* PSD-95 family MAGUKs are essential for anchoring AMPA and NMDA receptor complexes at the postsynaptic density. *Proc. Natl. Acad. Sci.* **112**, E6983–E6992 (2015).
  131. Cathala, L., Holderith, N. B., Nusser, Z., DiGregorio, D. A. & Cull-Candy, S. G. Changes in synaptic structure underlie the developmental speeding of AMPA receptor-mediated EPSCs. *Nat. Neurosci.* **8**, 1310–1318 (2005).
  132. Muller, D. & Nikonenko, I. Dynamic presynaptic varicosities: A role in activity-dependent synaptogenesis. *Trends Neurosci.* **26**, 573–575 (2003).
  133. Kondo, M. Molecular mechanisms of experience-dependent structural and functional plasticity in the brain. *Anat. Sci. Int.* **92**, 1–17 (2017).
  134. Waites, C. L., Craig, A. M. & Garner, C. C. Mechanisms of Vertebrate Synaptogenesis. *Annu. Rev. Neurosci.* **28**, 251–274 (2005).
  135. Munz, M. *et al.* Rapid Hebbian axonal remodeling mediated by visual stimulation. *Nat. Neurosci.* **344**, 904–909 (2014).
  136. Ruthazer, E. S., Li, J. & Cline, H. T. Stabilization of axon branch dynamics by synaptic maturation. *J. Neurosci.* **26**, 3594–3603 (2006).
  137. Matsuzaki, M., Honkura, N., C. R. Ellis-Davies, G. & Kasai, H. Structural basis of long-term potentiation in single dendritic spines. *Nature* **429**, 761–766 (2004).
  138. Südhof, T. C. Towards an Understanding of Synapse Formation.

- Neuron* **100**, 276–293 (2018).
139. Meyer, D., Bonhoeffer, T. & Scheuss, V. Balance and stability of synaptic structures during synaptic plasticity. *Neuron* **82**, 430–443 (2014).
  140. Chen, S. K., Badea, T. C. & Hattar, S. Photoentrainment and pupillary light reflex are mediated by distinct populations of ipRGCs. *Nature* **476**, 92–96 (2011).
  141. Kopp, M. D. A., Meissl, H., Dehghani, F. & Korf, H.-W. The pituitary adenylate cyclase-activating polypeptide modulates glutamatergic calcium signalling: investigations on rat suprachiasmatic nucleus neurons. *J. Neurochem.* **79**, 161–171 (2001).
  142. Choquet, D. Linking nanoscale dynamics of AMPA receptor organization to plasticity of excitatory synapses and learning. *J. Neurosci.* **38**, 9318–9329 (2018).
  143. Humeau, Y. *et al.* Hippocampal LTP and contextual learning require surface diffusion of AMPA receptors. *Nature* **549**, 384–388 (2017).
  144. Huganir, R. L. & Nicoll, R. A. AMPARs and synaptic plasticity : The last 25 years Perspective AMPARs and Synaptic Plasticity : The Last 25 Years. *Neuron* **80**, 704–717 (2016).
  145. Fields, R. D. A new mechanism of nervous system plasticity : activity-dependent myelination. *Nat. Publ. Gr.* **16**, 756–767 (2015).
  146. Lall, G. S. *et al.* Distinct contributions of rod, cone, and melanopsin photoreceptors to encoding irradiance. *Neuron* **66**, 417–428 (2010).

147. Güler, A. D. *et al.* Melanopsin cells are the principal conduits for rod-cone input to non-image-forming vision. *Nature* **453**, 102–105 (2008).
148. Lucas, R. J. *et al.* Diminished pupillary light reflex at high irradiances in melanopsin-knockout mice. *Science* (80-. ). **299**, 245–247 (2003).
149. Myung, J. *et al.* GABA-mediated repulsive coupling between circadian clock neurons in the SCN encodes seasonal time. *Proc. Natl. Acad. Sci.* **112**, E3920–E3929 (2015).
150. Farajnia, S., van Westering, T. L. E., Meijer, J. H. & Michel, S. Seasonal induction of GABAergic excitation in the central mammalian clock. *Proc. Natl. Acad. Sci.* **111**, 9627–9632 (2014).
151. Ono, D., Honma, K. ichi, Yanagawa, Y., Yamanaka, A. & Honma, S. GABA in the suprachiasmatic nucleus refines circadian output rhythms in mice. *Commun. Biol.* **2**, 1–12 (2019).
152. Horellou, S., Pascual, O., Triller, A. & Marty, S. Adaptive and non-adaptive changes in activity-deprived presynaptic terminals. *Eur. J. Neurosci.* **39**, 61–71 (2014).
153. Zito, K. & Svoboda, K. Activity-dependent synaptogenesis in the adult mammalian cortex. *Neuron* **35**, 1015–1017 (2002).
154. Altimus, C. M. *et al.* Rod photoreceptors drive circadian photoentrainment across a wide range of light intensities. *Nat. Neurosci.* **13**, 1107–1112 (2010).
155. Kirkby, L. A. & Feller, M. B. Intrinsically photosensitive ganglion cells contribute to plasticity in retinal wave circuits. *Proc. Natl. Acad. Sci. U.*

- S. A. **110**, 12090–12095 (2013).
156. Arroyo, D. A., Kirkby, L. A. & Feller, M. B. Retinal waves modulate an intraretinal circuit of intrinsically photosensitive retinal ganglion cells. *J. Neurosci.* **36**, 6892–6905 (2016).
157. Webb, I. C., Coolen, L. M. & Lehman, M. N. NMDA and PACAP Receptor Signaling Interact to Mediate Retinal-Induced SCN Cellular Rhythmicity in the Absence of Light. *PLoS One* **8**, 1–11 (2013).
158. Mure, L. S. *et al.* Diurnal transcriptome atlas of a primate across major neural and peripheral tissues. *Science (80-. )*. **359**, 1–20 (2018).